This document was prepared for the ETI by third parties under contract to the ETI. The ETI is making these documents and data available to the public to inform the debate on low carbon energy innovation and deployment.

Programme Area: Marine

Project: PerAWAT

Title: Experimental and Computation Investigations into Ducted Porous Discs and Rotors at Low Blockage

Abstract:

A number of experimental and computational investigations carried out on actuator discs and model scale tidal turbines are documented in this report. The first of these is a combined experimental and computational study of the effect of a duct on the performance and wake of a tidal turbine. The second investigation involves a comparison of the software package 'GH Tidal Bladed' against experimental measurements of rotor performance in low blockage flow. A comprehensive set of wake flow properties have been calculated from the test results by GL Garrad Hassan, which are included in the Appendix.

Context:

The Performance Assessment of Wave and Tidal Array Systems (PerAWaT) project, launched in October 2009 with £8m of ETI investment. The project delivered validated, commercial software tools capable of significantly reducing the levels of uncertainty associated with predicting the energy yield of major wave and tidal stream energy arrays. It also produced information that will help reduce commercial risk of future large scale wave and tidal array developments.

Disclaimer:
The Energy Technologies Institute is making this document available to use under the Energy Technologies Institute Open Licence for Materials. Please refer to the Energy Technologies Institute website for the terms and conditions of this licence. The Information is licensed 'as is' and the Energy Technologies Institute excludes all representations, warranties, obligations and liabilities in relation to the Information to the maximum extent permitted by law. The Energy Technologies Institute is not liable for any errors or omissions in the Information and shall not be liable for any loss, injury or damage of any kind caused by its use. This exclusion of liability includes, but is not limited to, any direct, indirect, special, incidental, consequential, punitive, or exemplary damages in each case such as loss of revenue, data, anticipated profits, and lost business. The Energy Technologies Institute does not guarantee the continued supply of the Information. Notwithstanding any statement to the contrary contained on the face of this document, the Energy Technologies Institute confirms that the authors of the document have consented to its publication by the Energy Technologies Institute.

Energy Technologies Institute

PerAWaT

WG4 WP3 D3: Experimental and computation investigations into ducted porous discs and rotors at low blockage

Authors	C. F. Fleming, S. C. McIntosh, R. H. J. Willden, T.Stallard, T. Feng
Version	1.1
Date	17/7/13

Revision History

Issue / Version	Issue Date	Summary
0.1	23/5/13	First draft for review by GH
0.2	31/5/13	Second draft following review by GH
1.0	4/6/13	Approved by GH
1.1	17/7/13	Error in Figure 29 corrected

Executive Summary

A number of experimental and computational investigations carried out on actuator discs and model scale tidal turbines are documented in this report. The first of these is a combined experimental and computational study of the effect of a duct on the performance and wake of a tidal turbine. In each study, the rotor is modelled as a porous disc, and tested with and without a duct, at blockage ratios based on the rotor area (4.8%) and total frontal area (6.3%) of the ducted device. Good agreement is observed between the predicted and measured results at low and medium levels of disc loading (corresponding to the practical operating range of an axial flow rotor). The observed effect of the duct is to reduce power coefficient (normalised on total frontal area) across all operating points. At low levels of disc loading, the duct increases the power density, i.e. power per unit rotor area. Computed and measured velocities downstream of the device show that the duct reduces the velocity deficit in the wake relative to an unducted turbine.

The second investigation involves a comparison of the software package ‘GH Tidal Bladed’ against experimental measurements of rotor performance in low blockage flow. A 1:70 scale axial flow rotor is tested at various elevations in sheared confined flow with a blockage ratio of 4.8%. Predicted thrust correlates well with measured thrust for moderate tip speed ratios, whereas at higher tip speed ratios, power is predicted well. A reduction in experimentally measured rotor power is noted for rotor operation near the free surface, which could be due to discrepancies between the assumed and actual undisturbed upstream velocity profiles.

The final study is concerned with the effects of channel bed proximity on the structure of a rotor wake. Wake measurements are taken for the aforementioned 1:70 scale rotor operating at two elevations in a sheared profile. No clear effect of flow shear or channel bed proximity is observable on downstream normalised velocity deficit or turbulence intensity.

A comprehensive set of wake flow properties have been calculated from the test results by GL Garrad Hassan, which are included in the Appendix.

1 Introduction

This document constitutes the third deliverable (D3) of working group 4, work package 3 (WG4 WP3) of the PerAWAT (Performance Assessment of Wave and Tidal Arrays) project funded by the Energy Technologies Institute (ETI). The project partners of this work package are University of Manchester (UoM), University of Oxford (UoO), Électricité de France (EdF) and Garrad Hassan (GH).

This deliverable consists of three investigations into tidal turbine performance at model scale. The first concerns the effect of a duct on turbine performance through matched experimental and computational models. In the second investigation, experimental measurements of turbine performance in low-blockage flow are compared with predictions by the software package 'GH Tidal Bladed'. The final study examines the effect of free-surface and bed proximity on rotor wake structure.

2 Effect of a Duct on Tidal Turbine Performance

2.1 Introduction

A computational study of a ducted tidal turbine carried out within the PerAWaT project by Fleming et al. (2011) indicated that a duct may have a detrimental effect on the power generated by a tidal turbine. In order to further investigate this finding, experimental work has recently been carried out by UoM using facilities at EdF. The duct for the model turbine is manufactured by rapid prototyping, and the rotor is represented by a series of porous discs of varying flow resistance. The performance of the ducted turbine is compared to the performance of two sets of bare porous discs. The first set of bare discs matches the area blockage of the rotor, while the second set matches the area blockage of the entire ducted device.

In a second exercise, the physical test results are compared with numerical predictions of ducted and unducted device performance produced by the Reynolds averaged Navier-Stokes (RANS) solver ANSYS Fluent. Efforts undertaken to reproduce the experimental conditions are described in this section.

2.2 Scale Model Geometry

2.2.1 Duct

A duct for a tidal turbine was designed in WG3 WP1 D2 within the following constraints:

1. the ratio of duct length L to duct diameter D is $L/D = 1.0$,
2. the duct is symmetric about the rotor plane (bi-directional),
3. the duct section is constructed from simple circular arcs.

The support structure for the duct and rotor was not considered. The resulting duct, labelled ‘Duct H’, had an external diameter of 0.4 m and was simulated in a numerical channel representing the EdF flume. The primary dimensions of the duct are indicated in Figure 1, where D_d denotes the diameter of the disc.

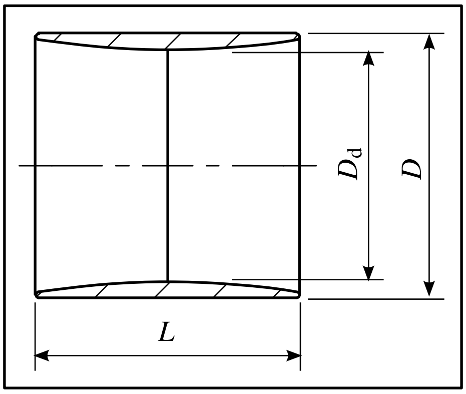

Figure 1: Schematic diagram of the duct showing primary dimensions.

For the current experimental study, the duct was scaled down uniformly to suit a 270 mm rotor. The resulting geometry is illustrated in Figure 2.

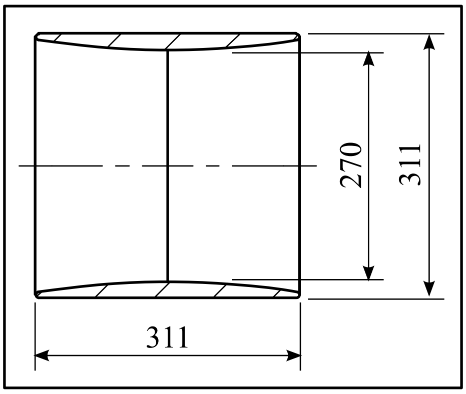

Figure 2: Schematic diagram of the scaled-down duct geometry, investigated in this work. Dimensions are in millimetres.

2.2.2 Rotor

Two unducted turbines are tested in addition to the ducted turbine. The first unducted turbine has a diameter of 270 mm, matching the rotor of the ducted turbine. The second unducted turbine has a diameter of 311 mm, matching the total blockage of the ducted turbine.

2.2.3 Channel

Testing is carried out in the EdF flume, which has a width of 1.5 m, a water depth of 0.8 m and a streamwise velocity of 0.55 m s^{-1} at the rotor centreline. These dimensions result in blockage values of 4.8% for the 0.27 m unducted turbine, and 6.3% for the 0.311 m ducted turbine.

2.3 Experimental Study

2.3.1 Physical Model of Rotor

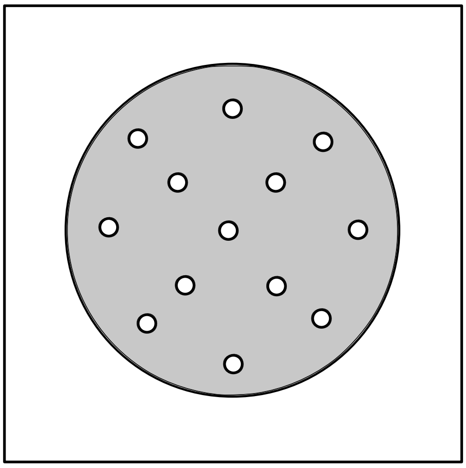

Figure 3: Schematic diagram of a porous disc.

For both the unducted and ducted turbines, the rotor is modelled physically by a porous disc (see Figure 3), which presents a similar resistance to flow in the streamwise direction for a given rotor operating point. Note that the swirl which would be imparted by a real rotor is not reproduced by a porous disc. For this investigation into the effect of a duct, swirl is considered to be of secondary importance relative to streamwise thrust.

The resistance of a porous disc is governed by its porosity, *k*, i.e. the ratio of open area (holes), A_{open} to solid area, A_{solid} .

$$k = \frac{A_{\text{open}}}{A_{\text{solid}}} \tag{1}$$

Hence a porous disc can represent a rotor at a single operating point only. In order to represent the full range of operating states, a set of discs of varying porosity must be used.

To enable comparison with the numerical porous disc model used in the computational study, the disc resistance is measured in terms of a local thrust coefficient, c_x , rather than porosity, *k*. The local thrust coefficient is defined as

$$c_x = \frac{T_{\text{disc}}}{\frac{1}{2}\rho A_{\text{ref}} u_{\text{disc}}^2} \tag{2}$$

where T_{disc} is the streamwise force on the disc, ρ is density, A_{ref} is a reference area (typically the projected frontal area of the device), and u_{disc} is the velocity at the disc plane.

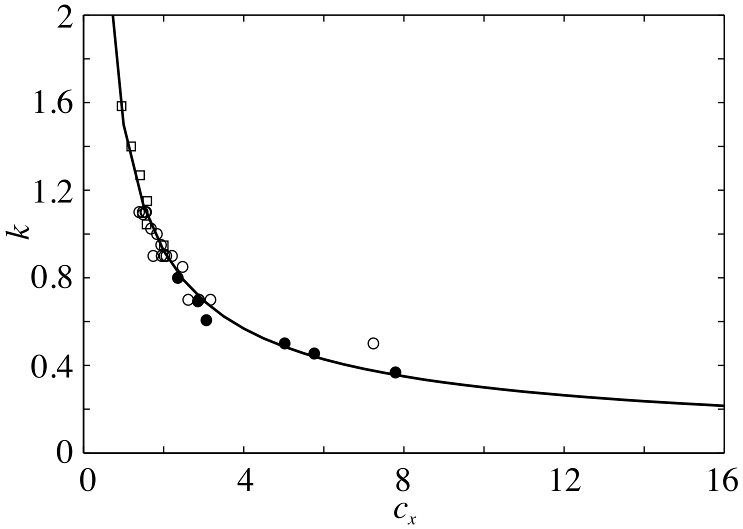

Figure 4: Variation of local thrust coefficient, c_x ,with porosity, *k*, for a range of hole diameters, adapted from WG4 WP3 D1.

The local thrust coefficient may be considered a unique property of the disc. This is demonstrated in Figure 4, where c_x is plotted against k for discs with different hole diameters.

Sets of 270 mm and 311 mm diameter discs are manufactured from 6 mm thick acrylic, with local thrust coefficients varying from $c_x = 0.6$ to $c_x = 16$. A detailed description of the discs is given in WG4 WP3 D1.

2.3.2 Support Structure

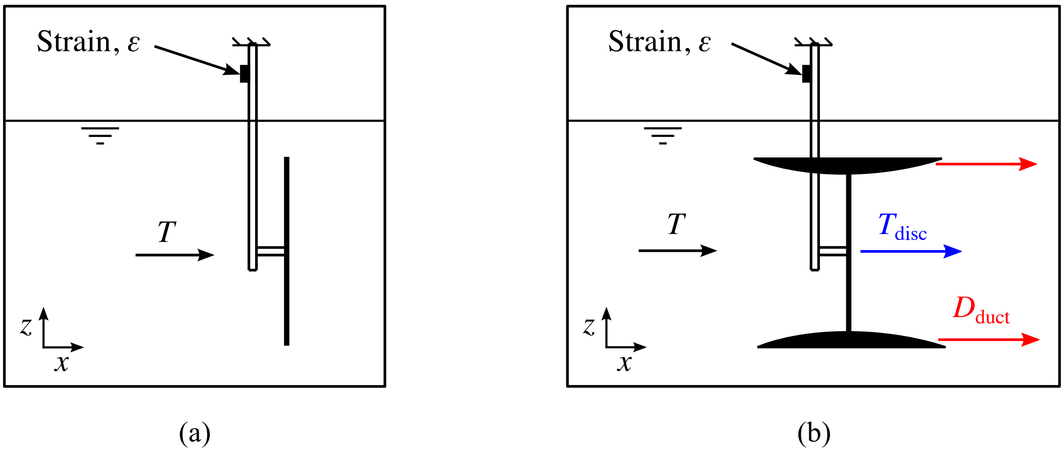

(a) (b)

Figure 5: Diagram of support tower for (a) the unducted disc and (b) the ducted disc.

The model turbine is supported from above by a 15 mm diameter tower with an embedded strain gauge, as indicated in Figure 5. Due to its position, the strain gauge measures the drag on the structure as well as the disc thrust. The drag on the tower, and duct where present, is subtracted from the total drag to yield the thrust force on the disc. Details of how this parasitic drag is quantified are given in WG4 WP3 D2.

One assumption in the isolation of duct drag is that this force is independent of the disc thrust. However, work by Belloni & Willden (2011) shows that a duct operates differently for high and low disc thrust. For high disc thrust, oncoming flow may separate from the leading edge of the duct, leading to an increase in pressure drag on that body. The computational model, which will be described in section 2.4, is used to check whether this effect is significant. Figure 6 shows that there is no consistent trend in the relationship between duct and disc thrust. The duct thrust measured at zero disc thrust is assumed to remain constant for the full range of disc thrust values.

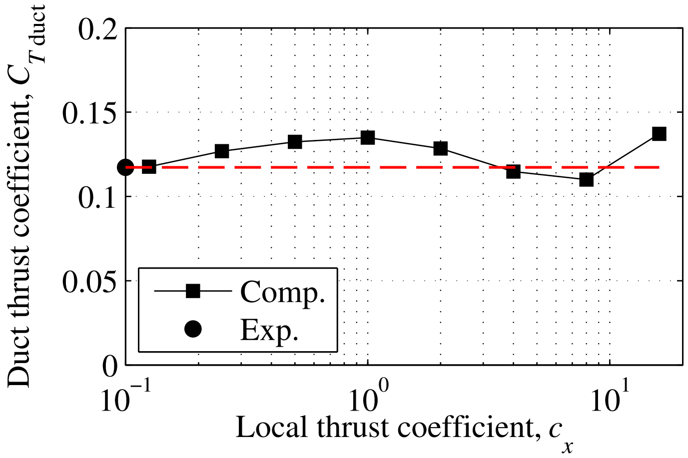

Figure 6: Variation of duct thrust coefficient against local disc thrust coefficient. The red broken line indicates the constant value of duct thrust which is assumed for all values of disc thrust.

2.3.3 Performance Measurement

Disc power P_{disc} is calculated from disc thrust T_{disc} using the formula

$$P_{\mathrm{disc}} = T_{\mathrm{disc}} u_{\mathrm{disc}} \tag{3}$$

where u_{disc} is the velocity at the disc. As it is not possible to directly measure the velocity at the disc, u_{disc} is instead estimated from the measured thrust. The local thrust coefficient c_x may be estimated from the global thrust coefficient, C_T, which is defined as

$$C_T = \frac{T_{\mathrm{disc}}}{\frac{1}{2}\rho A_{\mathrm{ref}} u_{\mathrm{ref}}^2} \tag{4}$$

where u_{ref} and A_{ref} are the reference velocity and reference area respectively. The reference velocity used in this experimental campaign is $u_{\text{ref}} = 0.55$ m s^{-1}, measured at hub height in the undisturbed flow upstream of the turbine. The reference area for a bare disc is the disc area. For a ducted disc, the total frontal area of the device is used as a reference area.

Linear momentum theory can be used to calculate the local thrust coefficient from the global thrust coefficient. The disc velocity can then be estimated by rearranging equation (2),

$$u_{\text{disc}} \approx \left[\frac{T_{\text{disc}}}{\frac{1}{2}\rho A_{\text{ref}} c_x} \right]^{\frac{1}{2}}. \tag{5}$$

Disc power may be calculated using equation (3).

In this report, thrust and power are normalised on the upstream velocity profile. Hence, differences in measured and computed performance due to discrepancies in the physical and simulated velocity profiles may be accounted for. The distributed thrust on the rotor can be normalised by the second moment of the upstream velocity profile (area-average of velocity squared)

$$C_T = \frac{T}{\frac{1}{2}\rho \int_{A_t} \left[u_\infty(y,z)\right]^2 \mathrm{d}A}, \tag{6}$$

where the integration is performed on the undisturbed profile far upstream of the rotor over the area which is intersected by the projected swept area of the turbine, A_r. Similarly, power can be normalised by the third moment of the upstream profile,

$$C_P = \frac{P}{\frac{1}{2}\rho \int_{A_t} \left[u_\infty(y,z)\right]^3 \mathrm{d}A}. \tag{7}$$

The velocity profile in the EdF flume has previously been measured in deliverables WG4 WP1 D3 and D4. The centreline velocity measured in D4 was closer to the nominal target of 0.55 m s^{-1} (the high velocity and low turbulence ‘U1 T0’ flow case) and was therefore chosen as the reference profile for these results, following discussion between University of Oxford and Garrad Hassan. The velocity has been measured at the vertical and horizontal midplanes of the flume only (i.e. in a ‘cross’ pattern). A two-dimensional profile has been extrapolated from this data, and is illustrated in Figure 7. This extrapolation is assumed to give an acceptably accurate velocity profile within the projected area of the device, i.e. the portion of the profile used for normalisation. The outline of a 0.311 m disc is marked in Figure 7; data outside this region is not used.

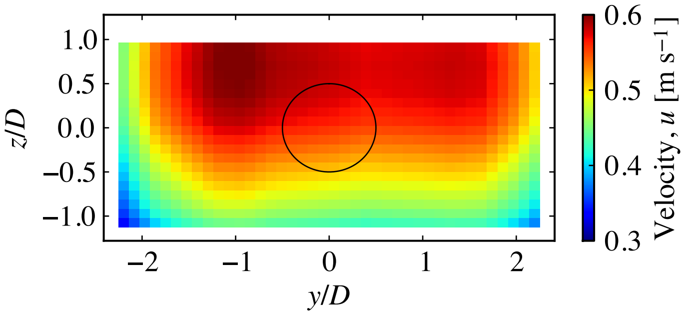

Figure 7: Extrapolated velocity profile used for normalising experimental results. The black circle marks the outline of a turbine of diameter $D = 0.311$ m.

2.3.4 Measurements

Thrust and flow velocity measurements are taken for each device (270 mm disc, 311 mm disc, ducted 270 mm disc). As discussed above, the thrust is measured via a strain gauge mounted on the supporting shaft. A velocity measurement is taken far upstream of the device (but still in the fully-developed flow region) at mid-depth in the flume, coinciding with the centreline of the disc. Horizontal and vertical velocity traverses are carried out at a series of downstream locations, detailed in Table 2.1 of WG4 WP3 D1. Quality control steps are described in WG4 WP3 D2.

2.3.5 Experimental Results

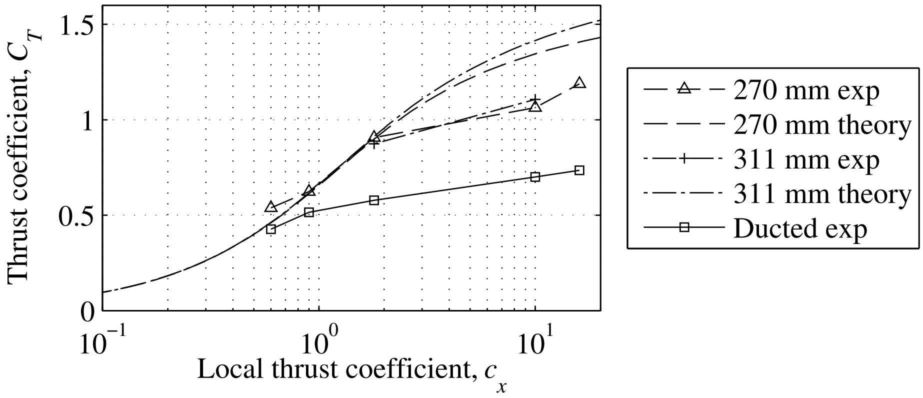

Figure 8: Comparison of experimentally measured thrust coefficient for the bare and ducted discs.

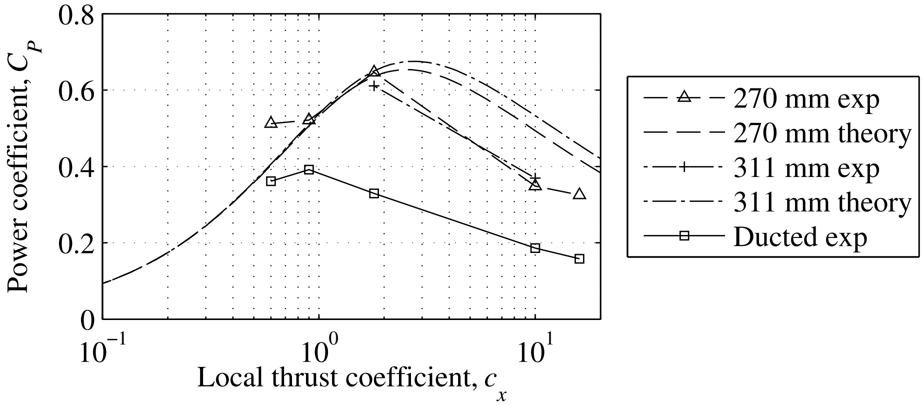

Figure 9: Comparison of experimentally measured power coefficient for the bare and ducted discs.

At low and medium levels of local thrust coefficient, unducted disc thrust and power agree well with theoretical results for an actuator disc operating at equivalent blockage (4.8% and 6.3%) calculated using linear momentum actuator disc theory (Houlsby, 2008). However the experimental results deviate from the analytical prediction at high local thrust coefficient (i.e. lower disc porosity). We suggest that this is because the low porosity discs approach the behaviour of a solid disc, with a resultant unsteady wake. Graham (1976) shows that the onset of this vortex-shedding mode for a rectangular porous strip occurs at $c_x \approx 4$, which is consistent with the current results. At Reynolds numbers of above $\mathrm{Re} = 10^3$, the drag of a solid circular disc asymptotes to $C_T = 1.17$ (Massey, 1998). The Reynolds number of the current tests is around $\mathrm{Re} = 10^5$. The lowest porosity 270 mm disc produces a thrust of $C_T = 1.23$ at a local thrust coefficient of $c_x = 16$, which lies closer to the solid disc limit than to the corresponding theoretical value of $C_T = 1.41$. This evidence would suggest that the porous disc physical model is not appropriate for such heavily loaded turbine conditions. However, we note that $c_x = 4$ is the realistic upper limit for turbine operation, so this restriction is of no practical consequence.

The ducted device produces much lower disc power than the bare discs when normalised on total projected frontal area. When renormalised on disc area, the ducted disc has a higher thrust coefficient than the unducted discs for high porosity (i.e. low local thrust coefficient). Although corresponding ducted disc power is improved, it only now approaches that of the bare discs. Note that there is a degree of uncertainty associated with ducted disc power, as velocity has not been measured inside the duct; rather it has been inferred from the local thrust coefficient as described in Section 2.3.3.

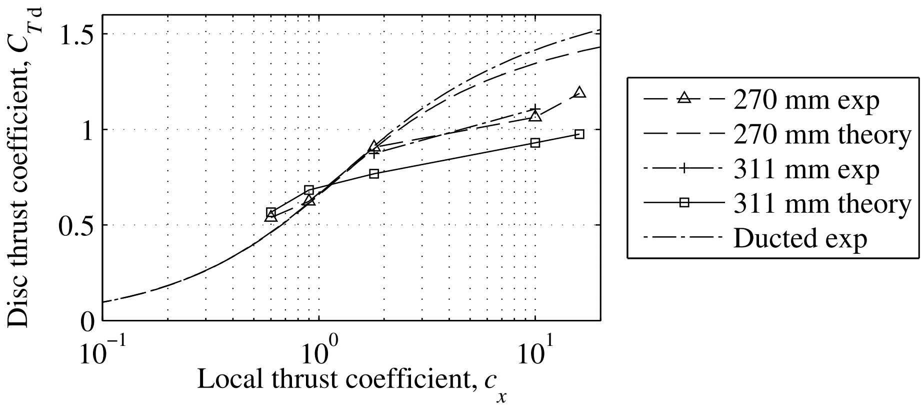

Figure 10: Reproduction of results in Figure 8, with ducted device thrust normalised on disc area.

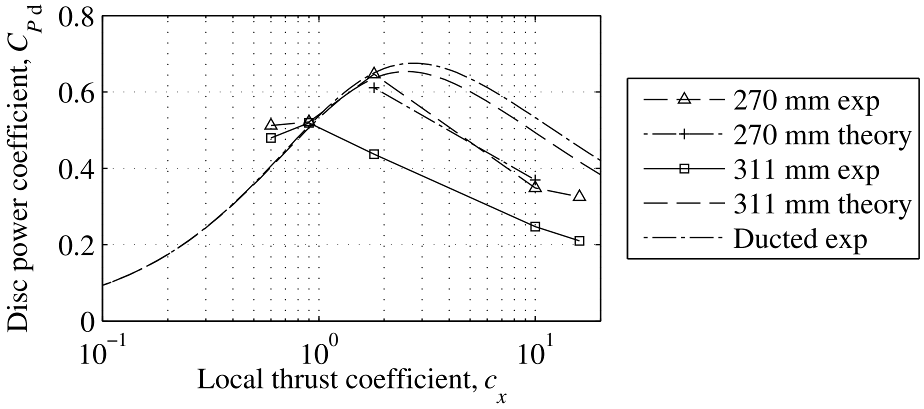

Figure 11: Reproduction of results in Figure 9, with ducted device power normalised on disc area.

2.4 Computational Study

2.4.1 Solver

The experimental model is replicated computationally using the Reynolds-averaged Navier-Stokes equations (RANS) solver ANSYS Fluent®. The k-ω SST model is used for turbulence closure, and the flow field is assumed to be steady.

2.4.2 Domain

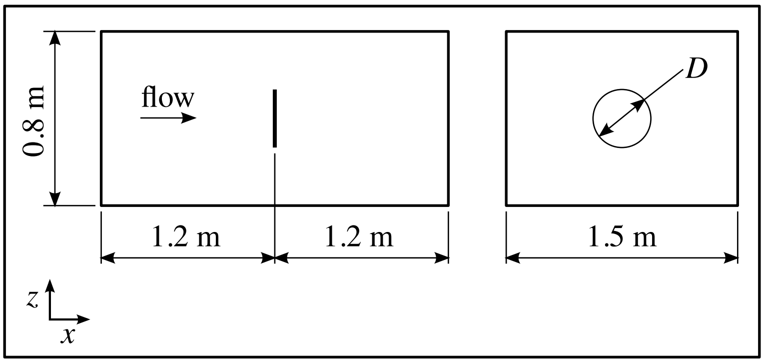

Figure 12: Side view and end view of the computational domain, showing an unducted disc in position. Discs of diameters $D = 0.27\ \text{m}$ and $D = 0.311\ \text{m}$ are simulated.

Side and end views of the computational domain are presented in Figure 12. The upstream and downstream distance of 1.2 m (~ 4*D*) is deemed to be sufficient based on findings from WG3 WP1 D2. A velocity profile is prescribed at the upstream boundary, and gauge pressure of $p = 0\ \text{Pa}$ is applied at the downstream boundary. The free surface is modelled as a rigid lid. Rough wall boundary conditions are applied at the sides and bottom boundaries of the domain to maintain the sheared velocity profile.

2.4.3 Velocity Profile

Testing is carried out in flow with a mid-depth velocity of $u_{\text{cl}} = 0.55\ \text{m s}^{-1}$. This is the only available measurement of the undisturbed velocity profile for the current experiments. However, the base flow in this flume has been characterised in previous work under WG4 WP1 D3 and D4. The profile corresponding to the high velocity and low turbulence 'U1 T0' flow case was used, as it has the same nominal centreline velocity as the current investigation (0.55 m s^{-1}). The profile from D3 was chosen, as a full grid of measurements were available. However a centreline velocity of only 0.52 m s^{-1} was achieved.

This velocity profile may be modelled as Poiseuille flow, where the time-averaged shear stress varies linearly from a value of $\tau = \tau_{\text{w}}$ at the channel bed to $\tau = 0$ Pa at the free surface. The theory behind Poiseuille flow is presented in WG3 WP1 D4. A Poiseuille velocity profile is fitted to the experimental data in Figure 13, yielding a bed friction coefficient of $c_f = 0.005$, where c_f is defined as

$$c_f = \frac{\tau_{\text{w}}}{\frac{1}{2}\rho u_{\text{ref}}^2}. \tag{8}$$

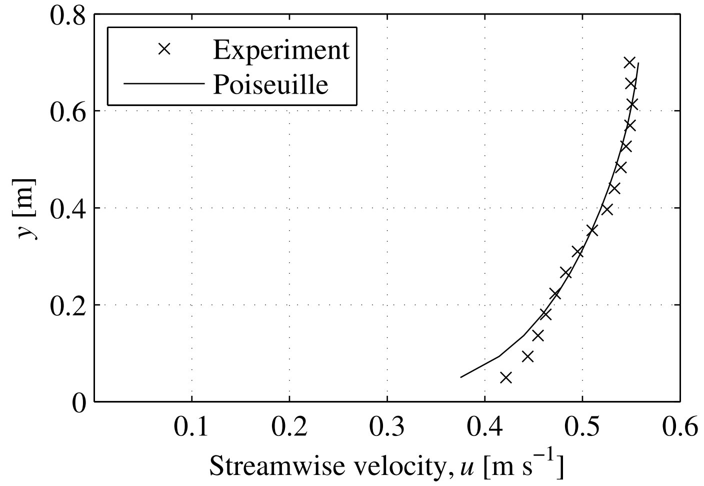

Figure 13: Velocity profile at the midplane of the EdF channel for a centreline velocity of $u_{\mathrm{cl}} = 0.52\ \mathrm{m\ s^{-1}}$, fitted with a Poiseuille flow velocity profile with wall friction coefficient of $c_{\mathrm{cl}} = 0.005$.

The measured centreline velocity for the current experiments is 0.55 m $\mathrm{s^{-1}}$. A Poiseuille flow velocity profile is assumed, and calculated for a wall friction coefficient of $c_f = 0.005$ and centreline velocity of $u = 0.55\ \mathrm{m\ s^{-1}}$. The resulting profile is illustrated in Figure 14, with the centreline velocity highlighted.

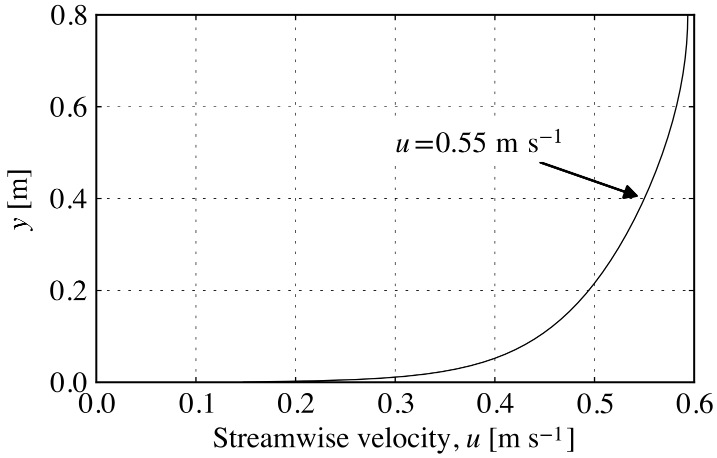

Figure 14: Assumed velocity profile for centreline velocity of $u = 0.55\ \mathrm{m\ s^{-1}}$.

A two-dimensional velocity profile is defined at the inlet boundary by ‘blending’ horizontal and vertical profiles from the sides and floor of the flume respectively. In other words, the velocity at a point $u(y, z)$ is calculated by multiplying the functions $u(y)$ and $u(z)$ together at that point. It has transpired during post-processing of the results of this study that the blending operation actually results in a slightly elevated centreline velocity. Hence the rotor performance is normalised on the computed velocity profile extracted three diameters upstream of the disc (rather than the blended analytical profile). Performance is normalised over the disc area projected onto this profile. The outline of a 0.311 m disc is marked on Figure 15 to highlight the corresponding normalisation area.

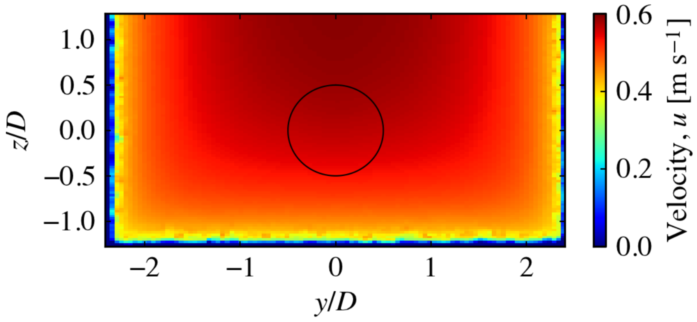

Figure 15: Extracted velocity profile used for normalising computational results. The black circle marks the outline of a turbine of diameter *D* = 0.311 m.

2.4.4 Rotor Model

The rotor is modelled as a numerical porous disc. Simulations are carried out for prescribed values of local thrust coefficient c_x corresponding to the physical porous discs. As a solution develops, the resistance of the numerical porous disc is altered until the target c_x is achieved and the flow field has converged.

2.4.5 Mesh

The domain is discretised with three-dimensional tetrahedral elements, following the method described in WG3 WP1 D2. Mesh resolution is based on work carried out in WG3 WP1 D2, where sensitivity studies have been carried out.

The maximum element size on the disc is $0.057D$, where D is the disc diameter. Element sizes on the duct, where present, vary from $0.057D$ in the midsection to $0.0072D$ at the leading and trailing edges. Seven layers of prismatic elements are used to resolve the sheared flow adjacent to the duct surfaces, with a wall-adjacent centroid height of order 1.0. The mesh resolution is illustrated in Figure 16 and Figure 17.

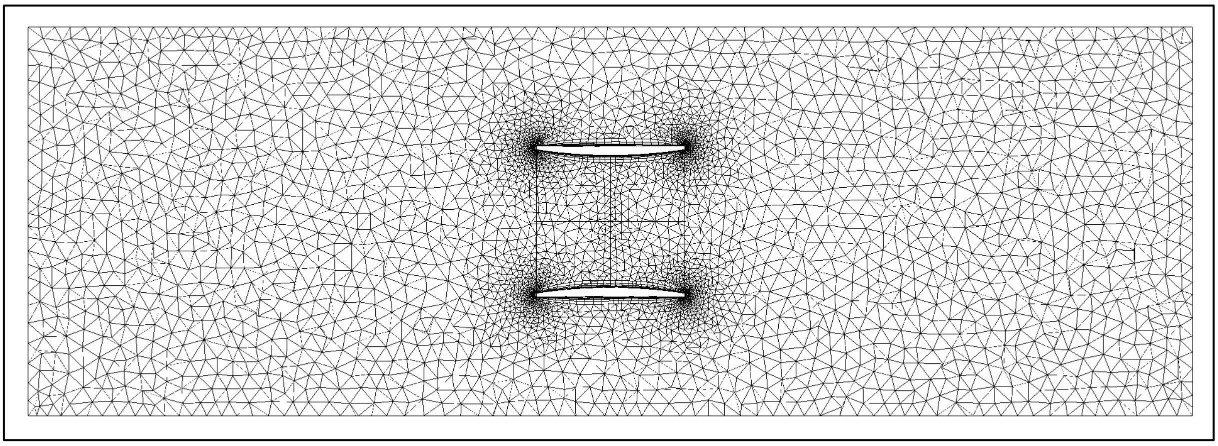

Figure 16: Section view through the vertical midplane of the computational domain showing general mesh element sizes.

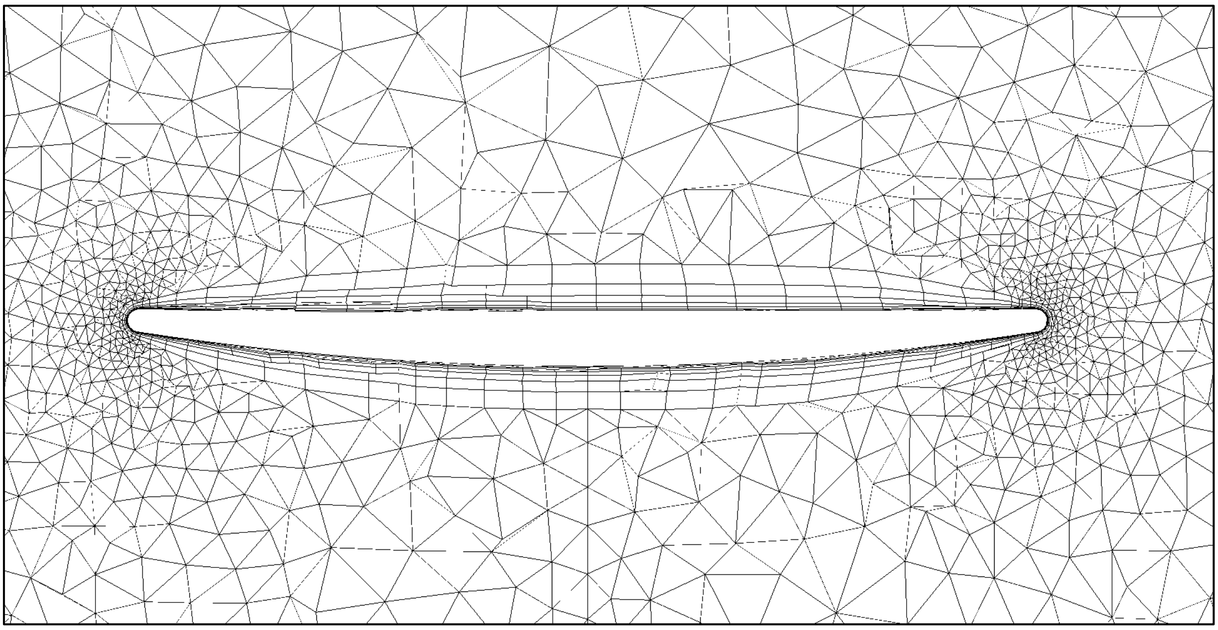

Figure 17: Close-up view of mesh, showing resolution in the vicinity of the duct.

2.4.6 Simulation Matrix

Table 1: A matrix of the simulations carried out in this study.

Disc	Duct	Local thrust coefficient, c_x								
270 mm	Yes	0	0.125	0.25	0.5	1	2	4	8	16
270 mm	No									
311 mm	No									

2.4.7 Computational Results

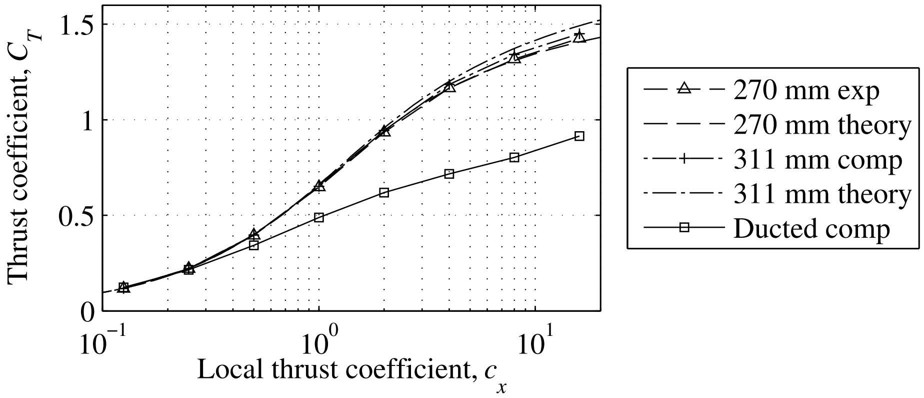

Figure 18: Comparison of computed thrust coefficient for the bare and ducted discs.

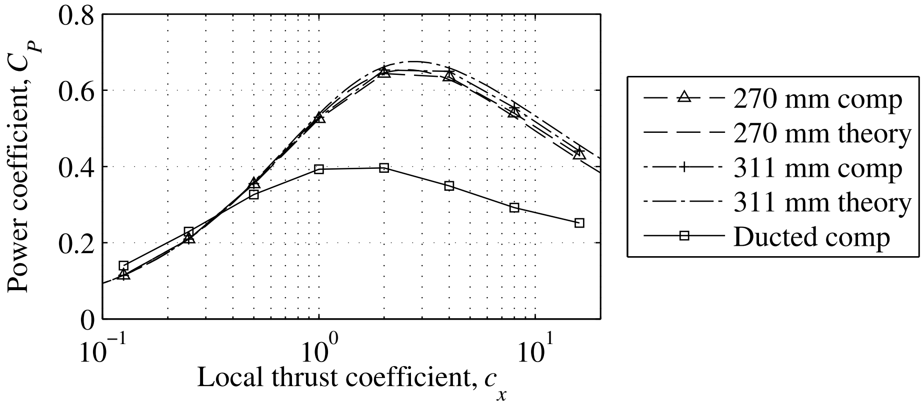

Figure 19: Comparison of computed power coefficient for the bare and ducted discs.

The computational results show the same trend as the experimental results presented earlier. The calculated performance of the bare discs agree well with linear momentum actuator disc theory (Houlsby et al, 2008). The small differences observed at high local thrust coefficient are likely to be due to viscous effects, which are not accounted for in the theoretical model.

In a similar result to the experimental study, the ducted disc performs less well than the bare discs. Note that duct performance is normalised on total projected frontal area of the device, including the duct. If performance is renormalised on the disc area only, the ducted disc outperforms the bare discs at low local thrust coefficient (high porosity). This is shown in Figure 18, where the new thrust and power coefficients are identified as $C_{T\mathrm{d}}$ and $C_{P\mathrm{d}}$ respectively. In other words, there is higher thrust and power per unit disc area for the ducted device in this region.

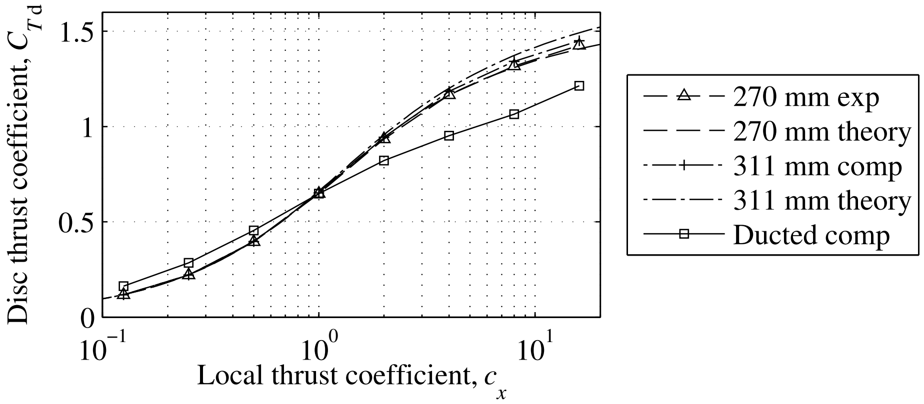

Figure 20: Reproduction of comparison in Figure 18 with duct performance renormalised on disc diameter.

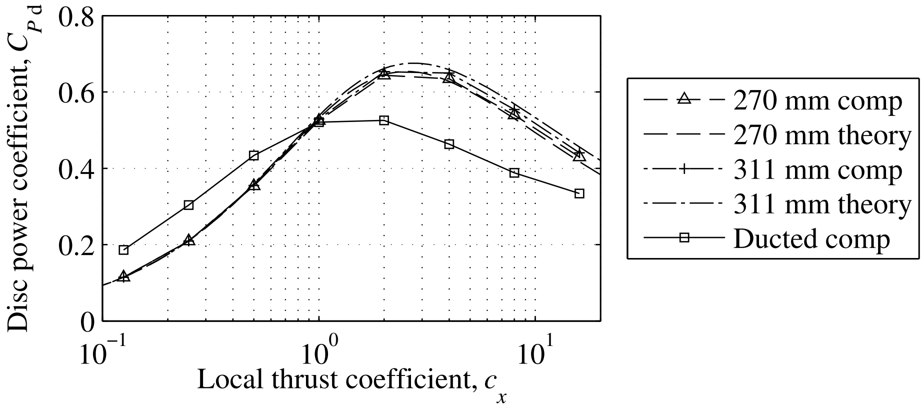

Figure 21: Reproduction of comparison in Figure 19 with duct performance renormalised on disc diameter.

2.5 Comparison of experimental and computational results

2.5.1 Thrust and power

The results of the experimental and computational studies are now compared in terms of device thrust and power. Both sets of bare disc results agree well with theory for low and medium levels of local thrust coefficient. At higher local thrust coefficients, the experimental results deviate from both the computational and theoretical results. It is suggested that this is due to the onset of vortex shedding, reported to occur above values of $c_x \approx 4$ for porous discs (Graham, 1976). Beyond this local thrust coefficient, the bare disc thrust coefficient may be tending towards the limiting value for a solid circular disc ($C_T = 1.17$).

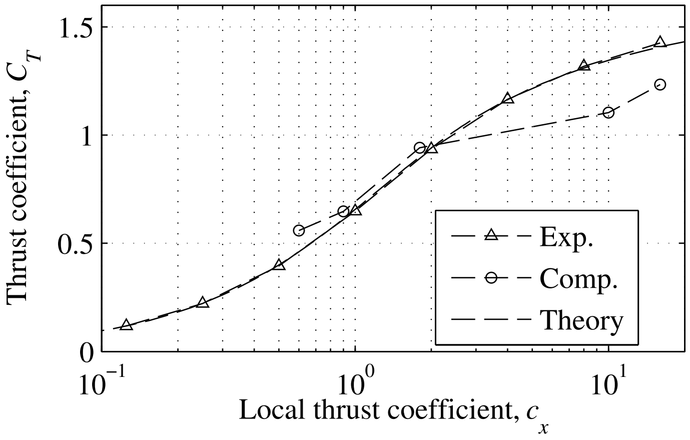

Figure 22: Comparisons of experimental measurements and computed predictions of thrust for the bare 270 mm disc.

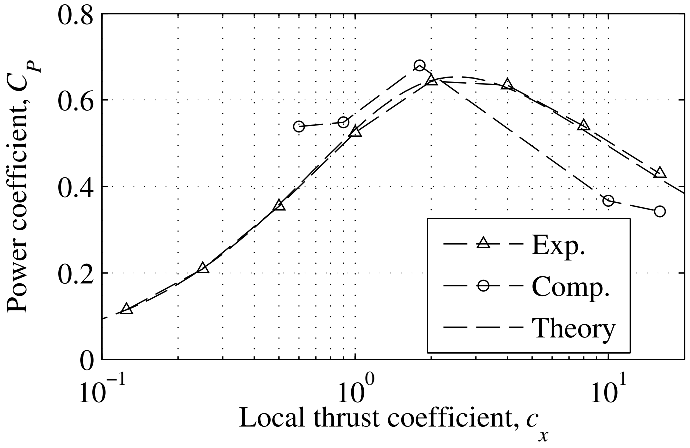

Figure 23: Comparisons of experimental measurements and computed predictions of power for the bare 270 mm disc.

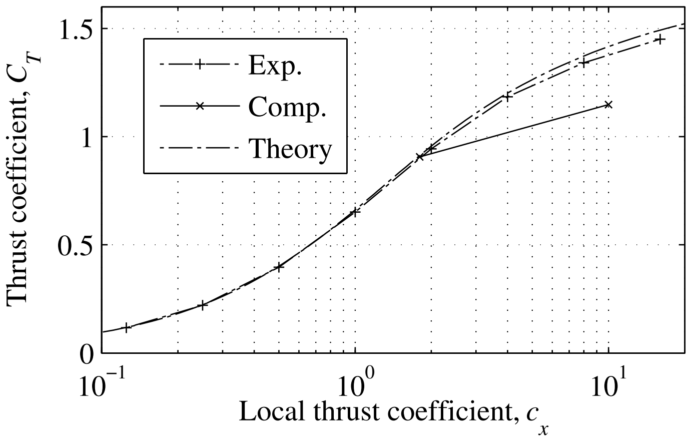

Figure 24: Comparisons of experimental measurements and computed predictions of thrust for the

bare 270 mm disc.

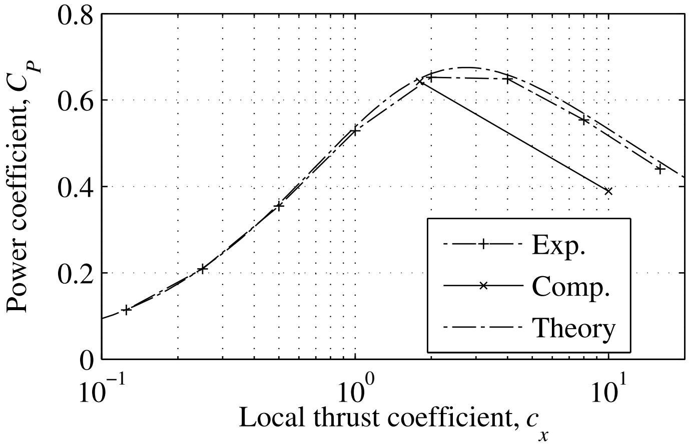

Figure 25: Comparisons of experimental measurements and computed predictions of power for the bare 270 mm disc.

Experimental and computational results for the ducted discs are compared in the following figures. Good agreement is observed in disc thrust coefficient (C_T, disc thrust normalised on total frontal area) and total thrust ($C_{T\ \mathrm{tot}}$, i.e. thrust on disc and duct normalised on total frontal area), for low values of local thrust coefficient. At high local thrust coefficients, the experimentally measured thrust falls below the computed thrust, following the trend observed for the unducted discs.

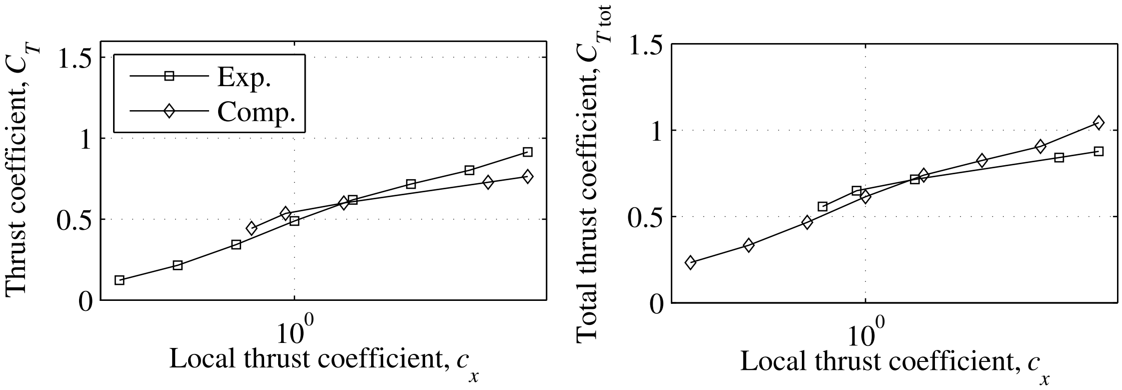

Figure 26: Comparisons of experimental measurements and computed predictions of thrust for the bare 270 mm disc.

In both the experimental and computational studies, the duct is generally observed to have a negative effect on disc power. The only situation where the duct is observed to increase performance is when considering power per unit disc area at low local disc thrust coefficient (high porosity).

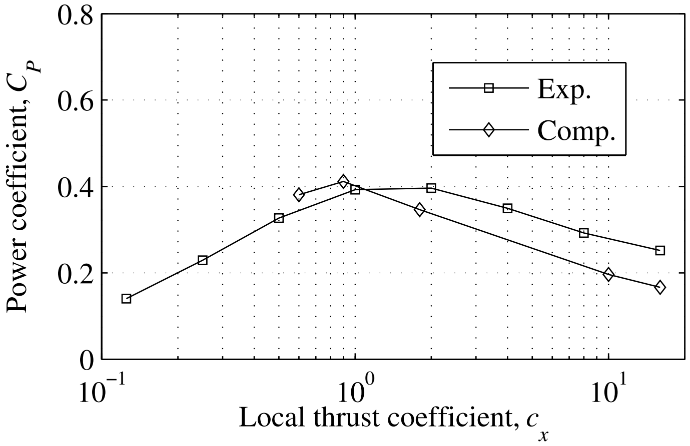

Figure 27: Comparisons of experimental measurements and computed predictions of power for the bare 270 mm disc.

2.5.2 Wake velocity

As part of the experimental study, wake velocity measurements are taken across the wake at a distance of 155 mm (approximately 0.5 duct diameters) downstream of the disc plane. Valid velocity comparisons can only be made where experimental and simulated device drag are similar. These conditions exist for the cases listed in Table 2. Additionally, it is preferable to make comparisons for both vertical wake traverses, $u_{\text{exp}} = f(z)$, and horizontal wake traverses, $u_{\text{exp}} = f(y)$, where available. Hence, wake comparisons are presented for test numbers 1.12, 1.31 and 1.22.

Table 2: Valid cases for wake velocity comparison.

Device	Test no.	$c_{x\,\text{exp}}$	$c_{x\,\text{comp}}$	$C_{T\,\text{exp}}$	$C_{T\,\text{comp}}$	$u_{\text{exp}} = f(z)$	$u_{\text{exp}} = f(y)$
270 mm bare	1.12	0.9	1.0	0.6473	0.6480	yes	yes
	1.13	1.8	2.0	0.9413	0.9348	yes	no
311 mm bare	1.31	1.8	2.0	0.9065	0.9438	yes	no
270 mm ducted	1.22	0.9	1.0	0.5347	0.4883	yes	yes
	1.23	1.8	2.0	0.6003	0.6188	yes	no

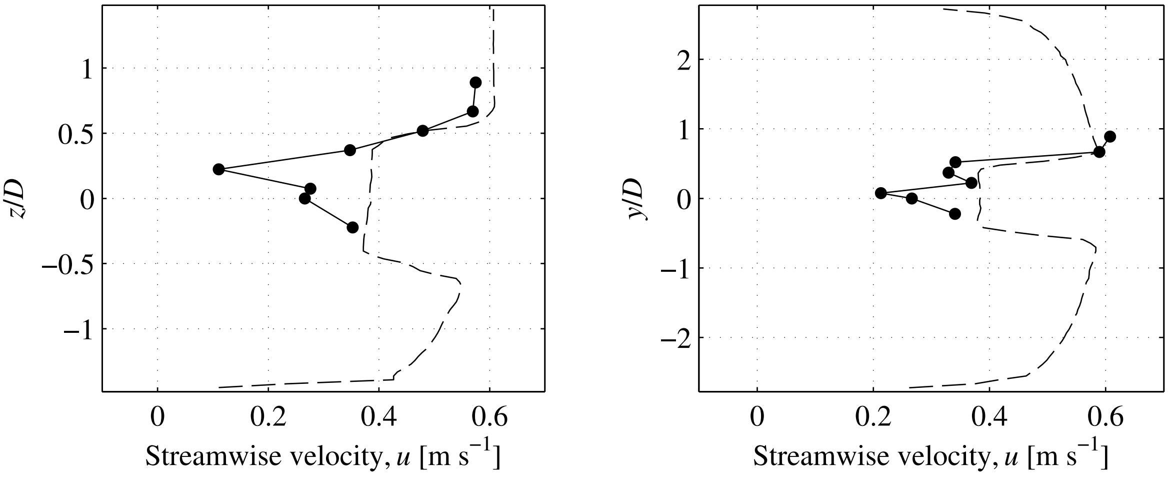

(a) (b)

Figure 28: Measured (solid line with dots) and computed (broken line) velocity at a downstream distance of x =0.155 m, for test 1.12 (270 mm disc at $c_{x\ \mathrm{exp}} = 0.9$).

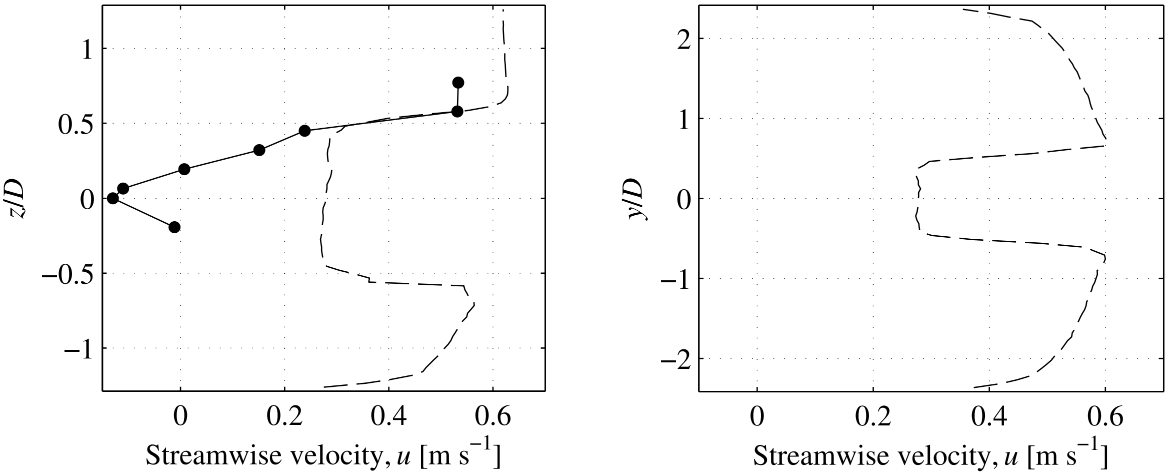

Figure 29: Measured (solid line with dots) and computed (broken line) velocity at a downstream distance of x =0.155 m, for test 1.31 (311 mm disc at $c_{x\ \mathrm{exp}} = 1.8$). Note that no horizontal traverse of experimental measurements was made for the 311 mm disc.

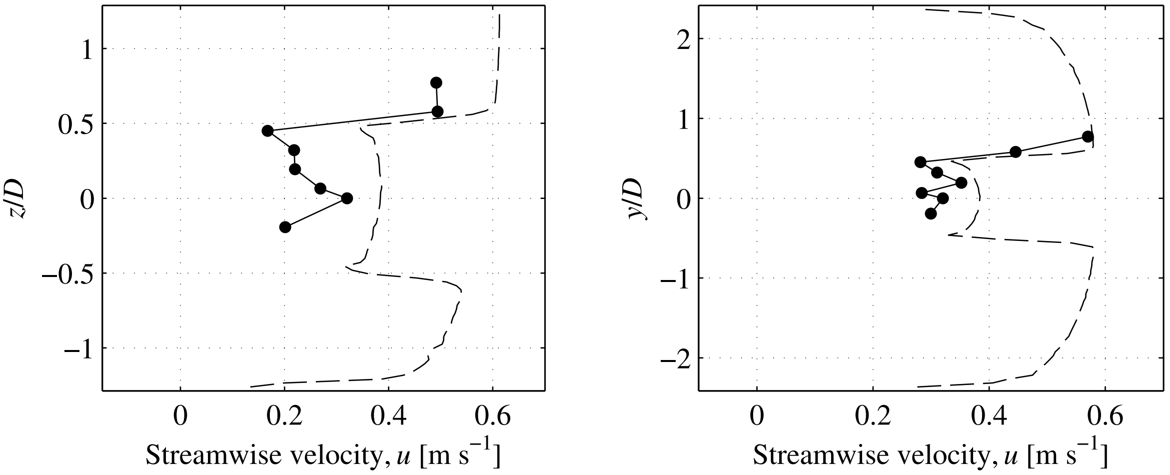

Figure 30: Measured (solid line with dots) and computed (broken line) velocity at a downstream distance of $x = 0.24$ m, for test 1.22 (ducted 270 mm disc at $c_{x\ \mathrm{exp}} = 0.9$). Note that wake measurements were taken further downstream for the ducted discs to avoid interference of the duct with the measurement device.

Vertical plots ($u = f(z)$) in each case show that measured velocity is lower than computed velocity. This is possibly due to the wake of the supporting tower, which has not been accounted for in the computational model. Horizontal plots ($u = f(y)$) show slightly better agreement, however it is still unclear why there is such variation in velocity measurements at a given downstream location.

The general effect of the duct, observed both experimentally and computationally, is to reduce the velocity deficit at the disc. The increased kinetic energy available to the disc would be expected to lead to an increase in extracted power. However, the duct also reduces the pressure differential across the disc (i.e. the disc thrust, c.f. Figure 8 and Figure 18), which reduces extracted power. The extracted power from a ducted turbine is the resultant of these two opposing effects.

3 Experimental Testing of Rotor

3.1 Introduction

A 1:70 scale axial flow rotor has previously been tested in WG4 WP2 at relatively high blockage (the vertical blockage was greater than 50%), and in close proximity to the bed and surface of the channel. The rotor in question however was designed for operation in unconstrained, uniform flow using GH Tidal Bladed. The objective of the current study is to measure the performance of the same rotor for lower levels of blockage and shear. This data will provide a useful reference for the rotor design tool.

3.2 Comparison with GH Tidal Bladed

3.2.1 Methods

The rotor from WG4 WP2 is a three-bladed axial flow rotor, with a diameter of 0.27 m. It is tested in the EdF flume, which measures 1.5 m in width and produces a flow of centreline velocity 0.55 m s^{-1} and depth 0.8 m. The resulting blockage ratio is 4.8%. Measurements of power and thrust are taken for the turbine in operation at hub heights of $0.25h$, $0.5h$ and $0.75h$ in the flume, where h is the depth of the flow.

These measurements are compared with numerical predictions by the software programme GH Tidal Bladed. This programme uses a routine based on the blade element momentum method to predict the thrust and power of an axial flow rotor, and uses a linear momentum model to calculate appropriate corrections for blockage effects. As an input, the code requires sectional lift and drag data for the rotor aerofoil section, at a Reynolds number corresponding to the rotor blade operating conditions.

The following comparison of measured and predicted results has been carried out by GL Garrad Hassan (GH). Two sets of aerofoil data are used, referred to as ‘Miley’ and ‘Marchwood’.

3.2.2 Results

Power and thrust are reported here as coefficients, normalised on the upstream velocity at hub height. Tests at each elevation are numbered according to Table 3. In the current tests, measurements were taken only of flume centreline velocity (i.e. at $z = 0.5h$), rather than at each hub height. Hence, the upstream hub height velocities were taken from the baseflow measurements in WG4 WP1 D4, where the velocity profile was measured at the vertical and horizontal midplanes, and are presented in Figure 31. The assumed hub height reference velocities (u_{ref}) are listed in Table 3.

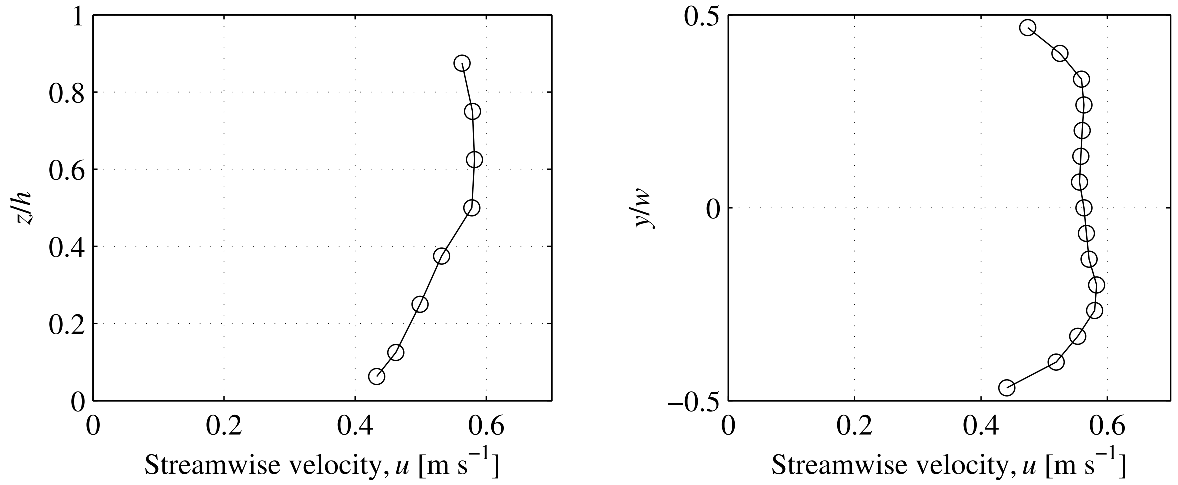

Figure 31: Vertical and horizontal velocity profiles measured in WG4 WP1 D4. *h* represents the depth of the flow, and *w* is the width of the channel.

Rotor performance is presented as a function of tip speed ratio, $\lambda = u_{\mathrm{tip}}/u_{\mathrm{ref}}$, where u_{tip} is the linear velocity of the rotor tip. Further details of the test procedure and quality control are given in deliverables WG4 WP3 D1 and D2.

Table 3: Reference velocity and test number corresponding to each elevation.

Elevation	u_{ref} [m s^{-1}]	Test number
0.25*h*	0.4969	2.3
0.5*h*	0.5589	2.1
0.75*h*	0.5879	2.2

Good agreement is observed in predicted and measured thrust for low and medium rotor elevation at tip speed ratios in the range $4 < \lambda < 5$. However, power is over-predicted in this range of rotor operation. Better agreement is observed in power at high tip speed ratio, but corresponding thrust is under-predicted.

While the experimental results at the low and medium rotor elevations are very similar, slightly higher thrust and slightly lower power is measured at the highest rotor position. These differences in thrust and power coefficients could be due to discrepancies between the assumed and actual upstream reference velocity.

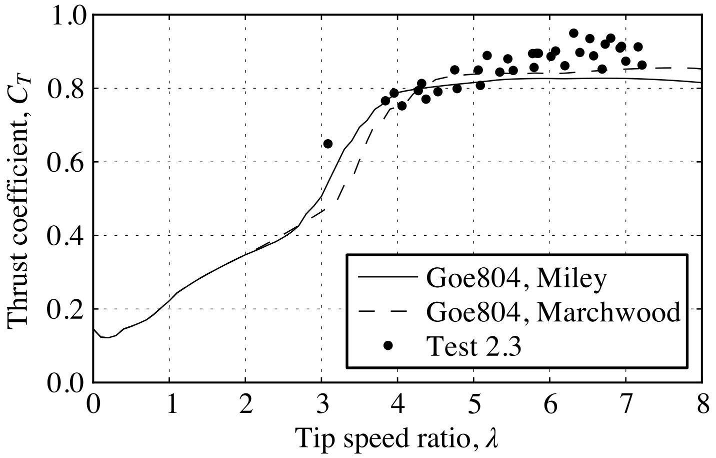

Figure 32: Comparison of measured (dots) and predicted (lines) thrust coefficient for test 2.3 $(z = 0.25h)$.

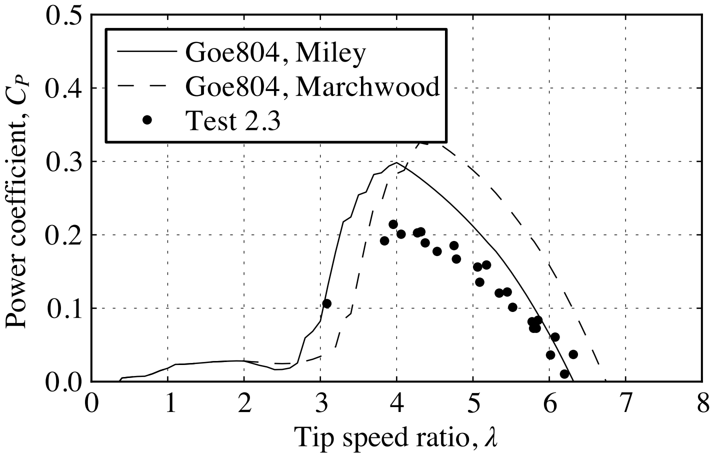

Figure 33: Comparison of measured (dots) and predicted (lines) power coefficient for test 2.3 $(z = 0.25h)$.

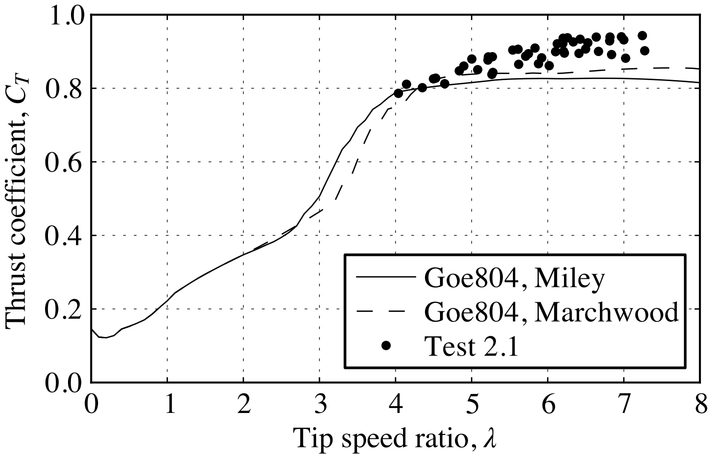

Figure 34: Comparison of measured (dots) and predicted (lines) thrust coefficient for test 2.1 $(z = 0.5h)$.

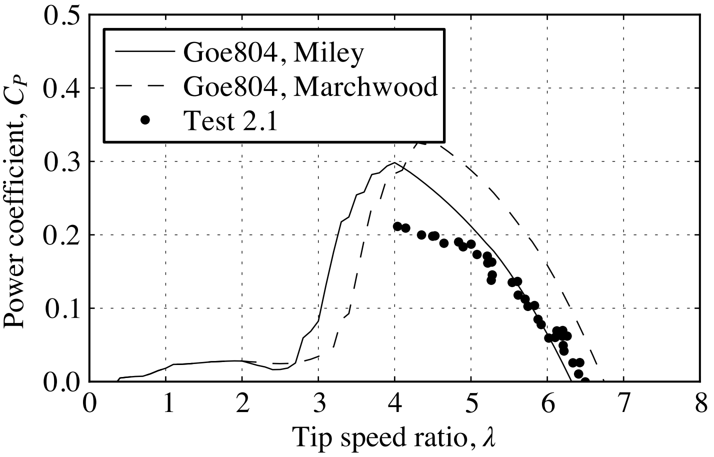

Figure 35: Comparison of measured (dots) and predicted (lines) power coefficient for test 2.1 $(z = 0.5h)$.

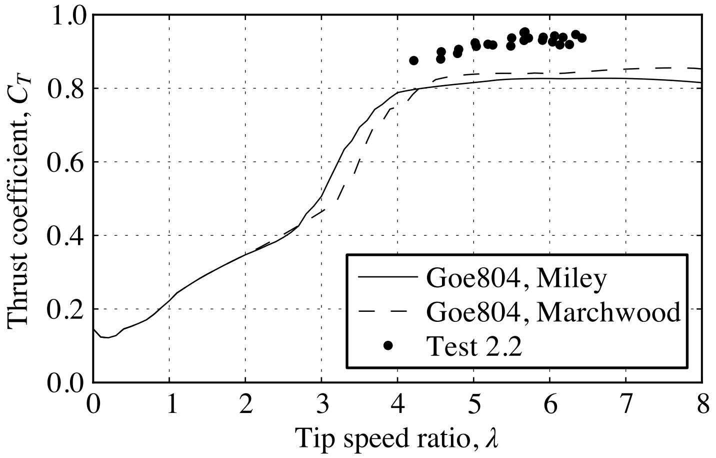

Figure 36: Comparison of measured (dots) and predicted (lines) thrust coefficient for test 2.2 $(z = 0.75h)$.

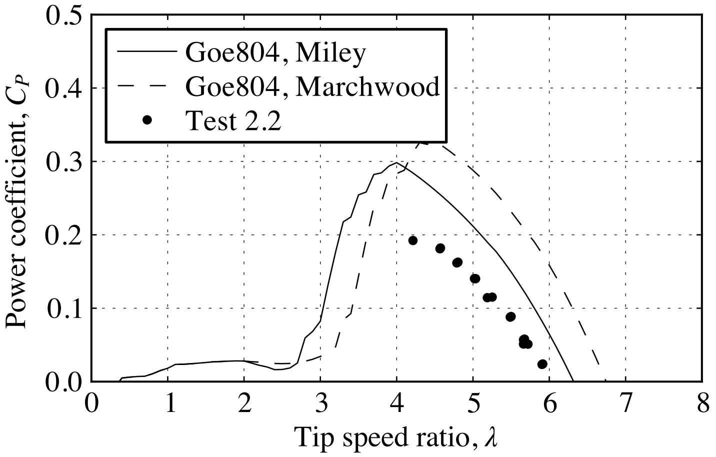

Figure 37: Comparison of measured (dots) and predicted (lines) power coefficient for test 2.2 $(z = 0.75h)$.

3.3 Effect of bounding surface on wake development

A second objective of the rotor testing was to determine the effect of boundary proximity on wake development. Wake velocity measurements were taken for a rotor in operation at hub heights of $0.25h$ and $0.5h$. Wake development is reported here in the form of a normalised velocity deficit, defined as

$$u_{\text{def nor}} = \frac{u_\infty(y,z) - u(x,y,z)}{u_\infty(y,z)} \tag{9}$$

where $u_\infty(y,z)$ is the undisturbed upstream velocity profile, and $u(x,y,z)$ is the velocity at a downstream measurement point. The upstream velocity was measured only at a single location ($u_\infty = 0.55\ \mathrm{m\ s^{-1}}$ at $y = 0,\ z = 0.5h$). As in Section 2.3.3, the velocity profile is extrapolated from measurements at the vertical and horizonal midplanes of the flume from WG4 WP1 D4. This assumed profile should be appropriate for normalisation of wake velocity measurements along the vertical and horizontal midplanes and along the flume centreline. This extrapolation will introduce some error into the normalisation of the horizontal velocity profile at the lower elevation ($z = 0.25h$).

Turbulence intensity is calculated from the unsteady velocity signal at each measurement point, using the formula

$$TI = \frac{u_{\mathrm{rms}}}{U} \tag{10}$$

where the root-mean-square of velocity, u_{rms}, is calculated from the directional fluctuations in velocity (denoted with a $'$ marker)

$$u_{\mathrm{rms}} = \sqrt{\frac{1}{3}\left(u'^2 + v'^2 + w'^2\right)} \tag{11}$$

and U is velocity magnitude,

$$U = \sqrt{u^2 + v^2 + w^2}\ . \tag{12}$$

3.3.1 Results

Comparisons of normalised velocity deficit $u_{\mathrm{def\ nor}}$ and turbulence intensity TI are presented below. No clear trend is observed in velocity profiles, which suggests that the normalisation upon the upstream velocity is an effective way of comparing rotor performance in different degrees of sheared flow.

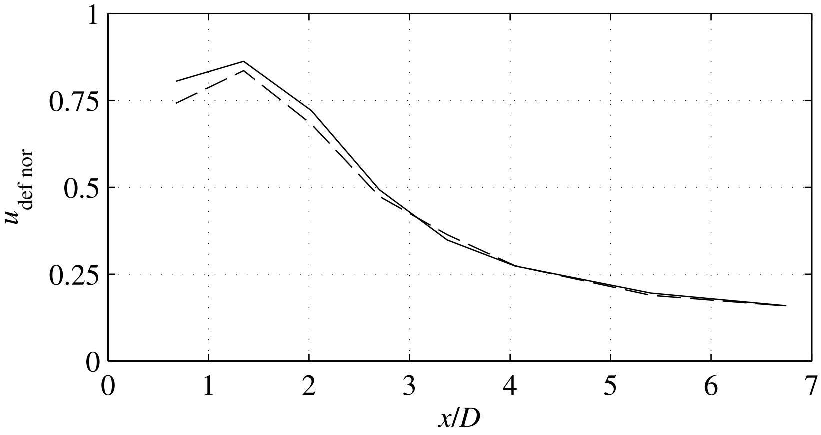

Figure 38: Comparison of normalised velocity deficit at $z = 0.25h$ (broken line) and $z = 0.5h$ (solid line).

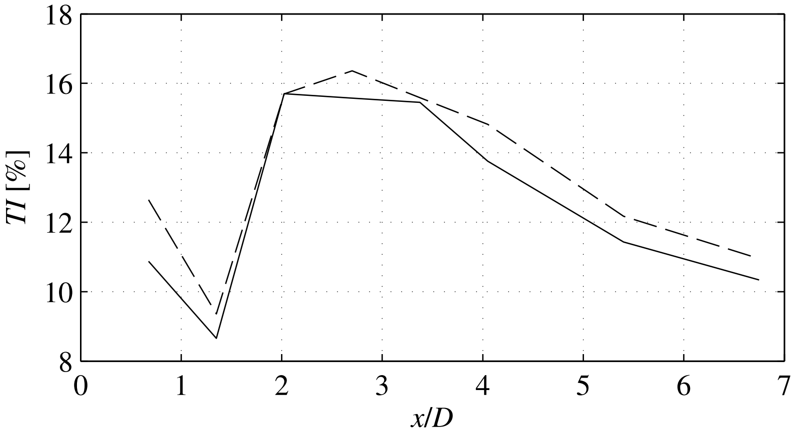

Figure 39: Comparison of turbulence intensity at $z = 0.25h$ (broken line) and $z = 0.5h$ (solid line).

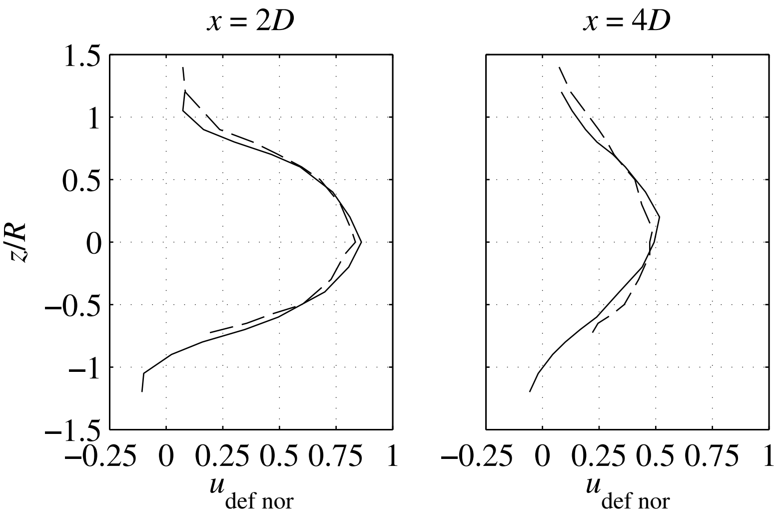

Figure 40: Comparison of normalised velocity deficit at $z = 0.25h$ (broken line) and $z = 0.5h$ (solid line) along the vertical midplane at two downstream locations.

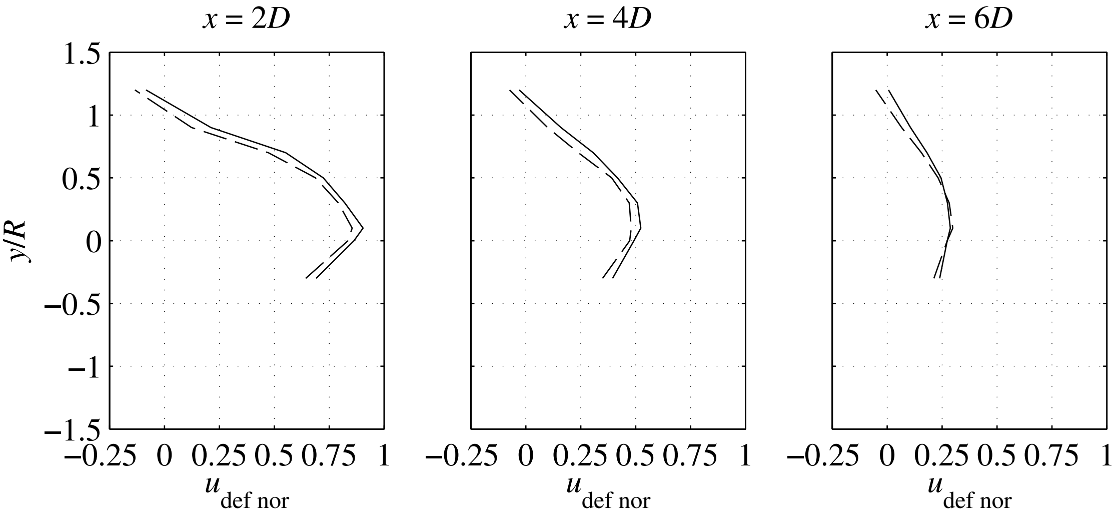

Figure 41: Comparison of normalised velocity deficit at $z = 0.25h$ (broken line) and $z = 0.5h$ (solid line) along the horizontal midplane at three downstream locations.

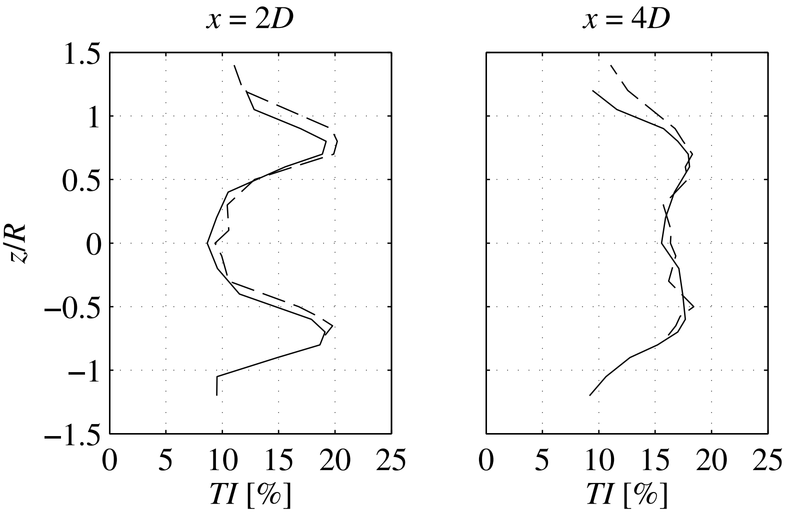

Figure 42: Comparison of turbulence intensity at $z = 0.25h$ (broken line) and $z = 0.5h$ (solid line) along the vertical midplane at two downstream locations.

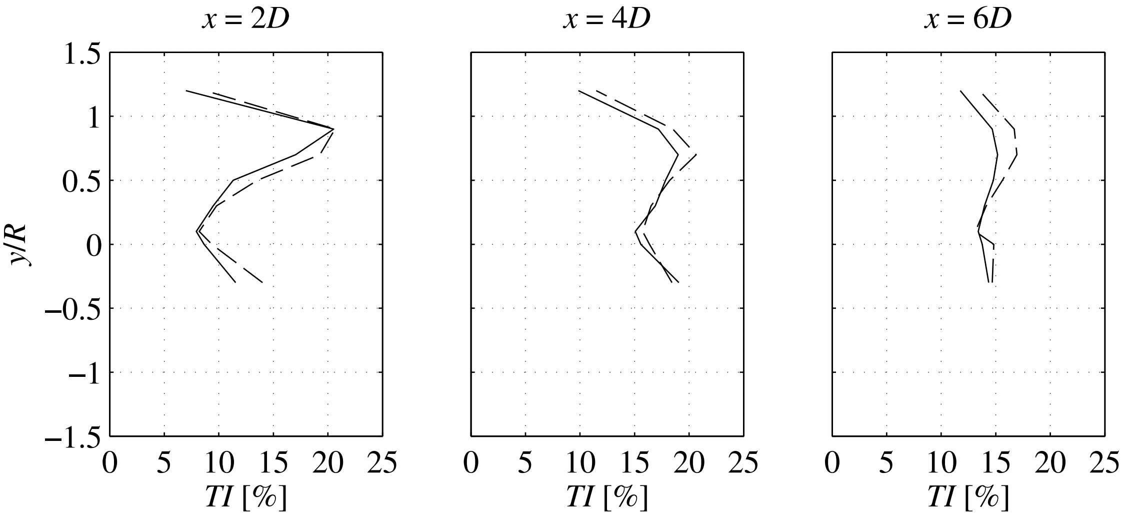

Figure 43: Comparison of turbulence intensity at $z = 0.25h$ (broken line) and $z = 0.5h$ (solid line) along the horizontal midplane at three downstream locations.

4 Conclusions

This report presents the results of experimental and computational studies into the effects of an external duct and boundary proximity on tidal turbine performance and wake development. The main findings of these results are presented below.

Complementary experimental and computational studies were carried out on ducted and unducted tidal turbines, where the rotor is modelled as a porous disc. Very good agreement was observed between experimental measurements and computational and theoretical predictions of unducted disc performance at low and medium loading. For the highest rotor loading states, the experimental results deviate from the expected performance. However, these highly loaded states are above the practical operating range of tidal turbines, and therefore the discrepancy is inconsequential.

The duct is generally observed to reduce disc power coefficient in experimental and computational results. However, it has been shown that the ducted disc has a higher power density, i.e. power per unit disc area, for low loading states.

In a second study, experiments were carried out on a 1:70 scale axial flow rotor at an area blockage ratio of 4.8% for performance comparison with the tidal turbine design code GH Tidal Bladed. The rotor was tested at different heights in the flume, to test the rotor under various upstream sheared flow conditions. Good agreement is observed in thrust coefficient for moderate tip speed ratios, whereas power coefficient is well matched at high tip speed ratios. The experimentally measured power coefficient is reduced at the highest rotor elevation, corresponding to the highest hub-height velocity and lowest degree of upstream shear. The cause of this unexpected result could be due to an error in the estimation of hub height velocity, which is based on measurements from a previous experimental campaign.

Finally, velocity and turbulence intensity measurements were taken along the centreline and in vertical and horizontal traverses downstream of the same rotor operating at two elevations in the flume. No clear trend was observed in normalised velocity deficit, suggesting that the normalisation method effectively accounts for the influence of a sheared incident flow and elevation. A comprehensive set of wake data, calculated by Garrad Hassan, is included in the Appendix.

5 References

Buvat, C., Stallard, T., Joly, A & Bodel, C. (2013) *Experiment data, quality controlled and delivered*, PerAWaT Report WG4 WP3 D2

Belloni, C. S. K and Willden, R. H. J. (2011) *Flow field and performance anal- ysis of bidirectional and open-centre ducted tidal turbines.* European Wave and Tidal Energy Conference, Southampton, UK.

Fleming, C. F., McIntosh, S. C., & Willden, R. H. (2011). *Design and analysis of a bi-directional ducted tidal turbine,* European Wave and Tidal Energy Conference, Southampton, UK.

Fleming, C. F., McIntosh, S. C., & Willden, R. H. (2012). *WG3 WP1 D4: Performance and Wake Structure of a Full-Scale Horizontal Axis Axial Flow Turbine.* University of Oxford.

Graham, J.M.R (1976). *Turbulent flow past a porous plate.* Journal of Fluid Mechanics, 73, pp 565-591 doi:10.1017/S002211207600150X

Houlsby, G.H., Draper, S. & Oldfield, M.L.G. (2008). *Application of linear mometum actuator disc theory to open channel flow.* Tech. Rep. OUEL 2296/08, University of Oxford.

Massey, B. S. (2008), *Mechanics of Fluids*, Stanley Thornes

McIntosh, S. C., Fleming, C. F., & Willden, R. H. (2010). *WG3 WP1 D1: Report on Model Setup for Horizontal Axis Axial Flow Turbines.* University of Oxford.

McIntosh, S. C., Fleming, C. F., & Willden, R. H. (2011). *WG3 WP1 D3: Performance and wake structure of a model horizontal axis axial flow turbine.* University of Oxford.

Stallard, T., Willden, R.H.J, McIntosh, S., Feng, T. (2012) *Design and specification of ducted disc experiments*, PerAWaT Report WG4 WG3 D1

6 Appendix

6.1 Introduction

Further wake statistics for the boundary proximity study in Section 3.3.1 are presented here. The figures have been provided by GL Garrad Hassan. The data in Sections 6.2 and 6.3 correspond to test series 3.1 and 3.2 respectively. In test series 3.1 the rotor is situated 0.4 m ($z = 0.5h$) above the channel bed, whereas for test series 3.2 it is located 0.2 m ($z = 0.25h$) above the channel bed. A list of wake parameters is presented in Table 4.

Table 4: List of wake parameters presented in the appendix.

Parameter	Symbol
Streamwise velocity	u
Lateral velocity	v
Vertical velocity	w
Normalised streamwise velocity deficit	$u_{\mathrm{def\ nor}}$
Reynolds stresses	$\overline{u'v'}$, $\overline{u'w'}$, $\overline{v'w'}$
Turbulence intensity	TI
Turbulent kinetic energy	TKE

For the vertical and lateral wake traverses, the following colour key is used.

Table 5: Wake location colour key.

Symbol and colour	Downstream distance
●	$x = 2D$
●	$x = 3D$
●	$x = 4D$
●	$x = 5D$
●	$x = 6D$

6.2 Test 3.1 - 0.4 m Elevation

6.2.1 Streamwise Velocity

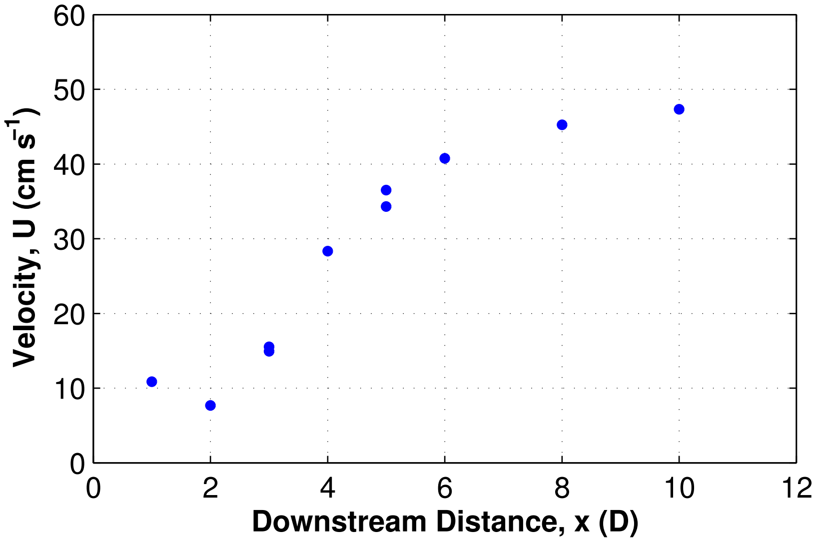

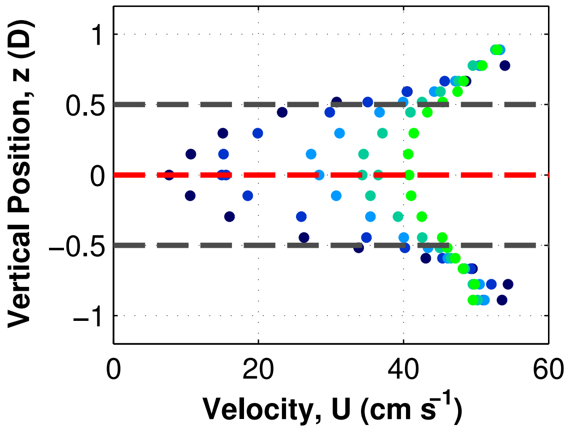

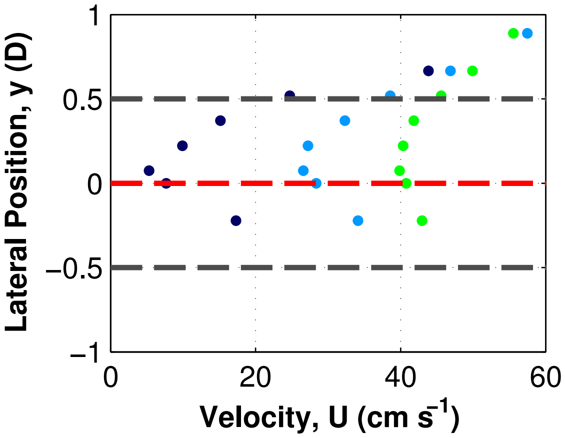

6.2.2 Lateral Velocity

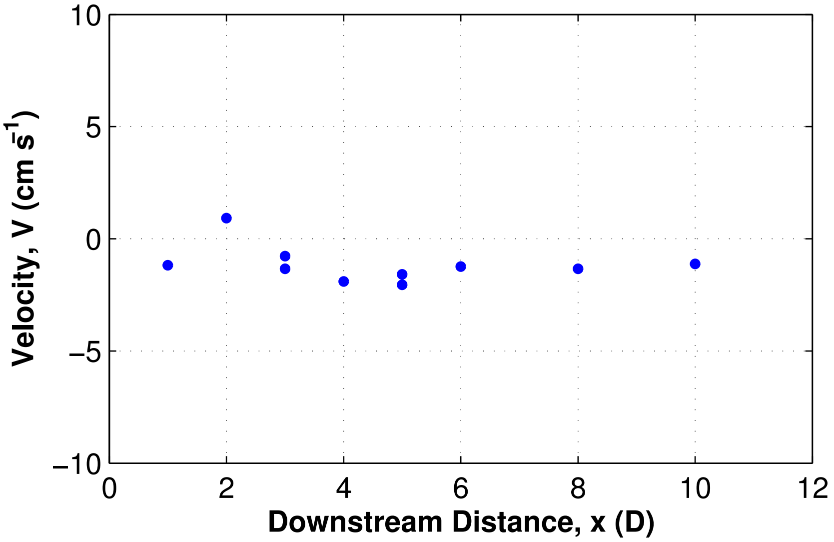

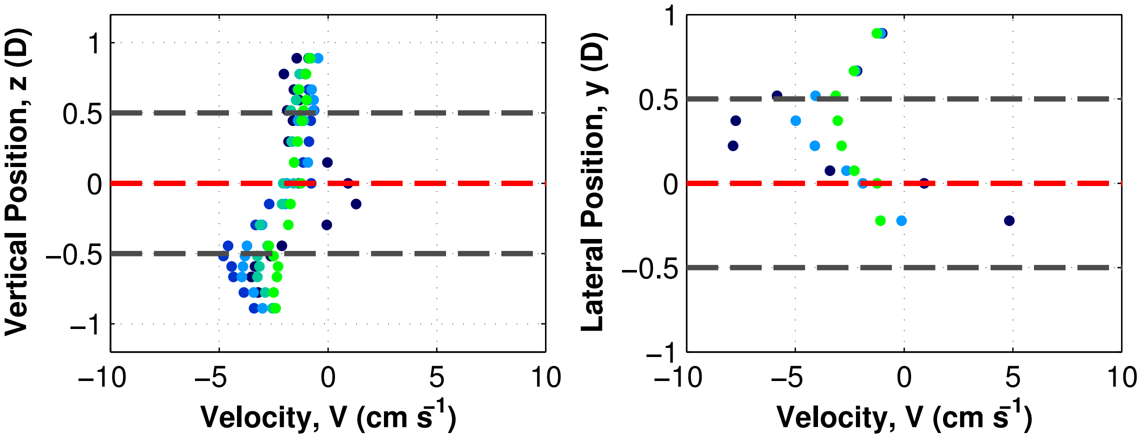

6.2.3 Vertical Velocity

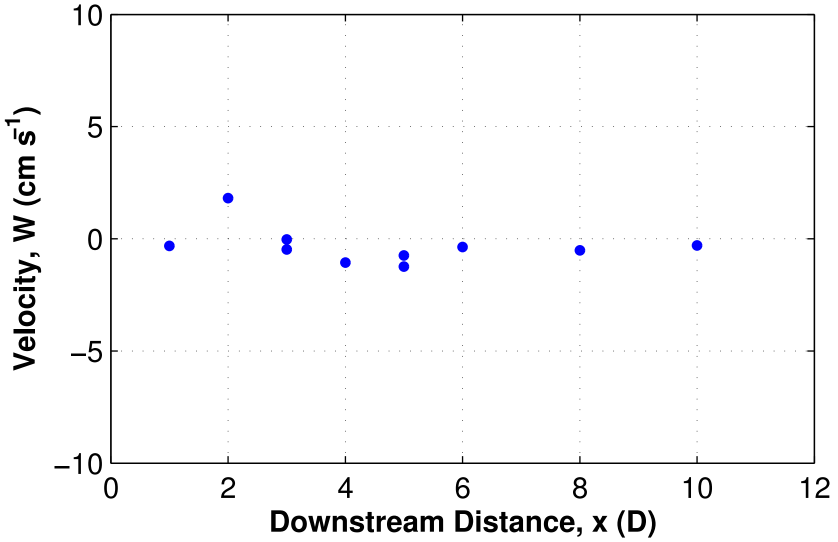

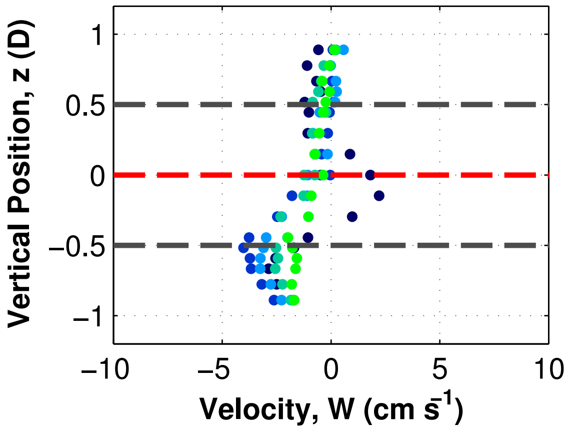

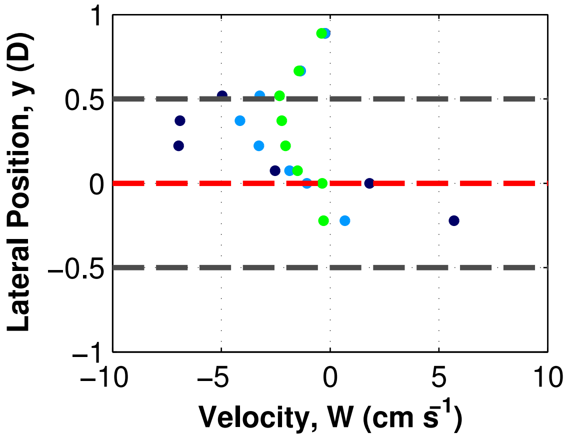

6.2.4 Normalised Streamwise Velocity Deficit

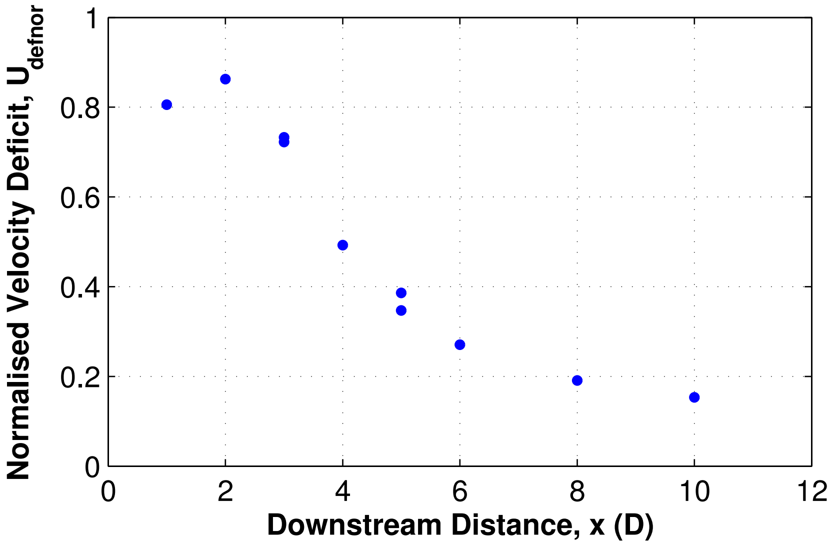

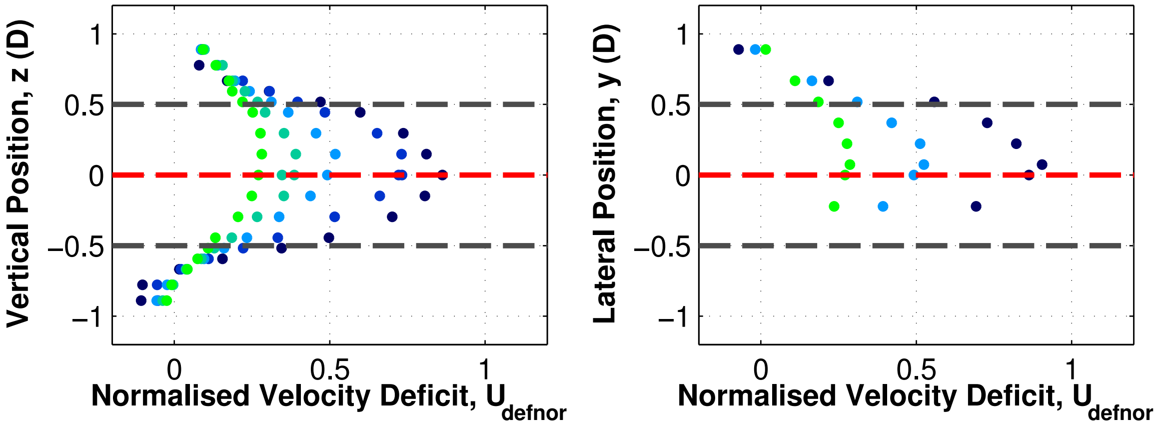

6.2.5 Reynolds stresses

The directional components of Reynolds stresses, $\overline{u'v'}$, $\overline{u'w'}$, and $\overline{v'w'}$, are presented here.

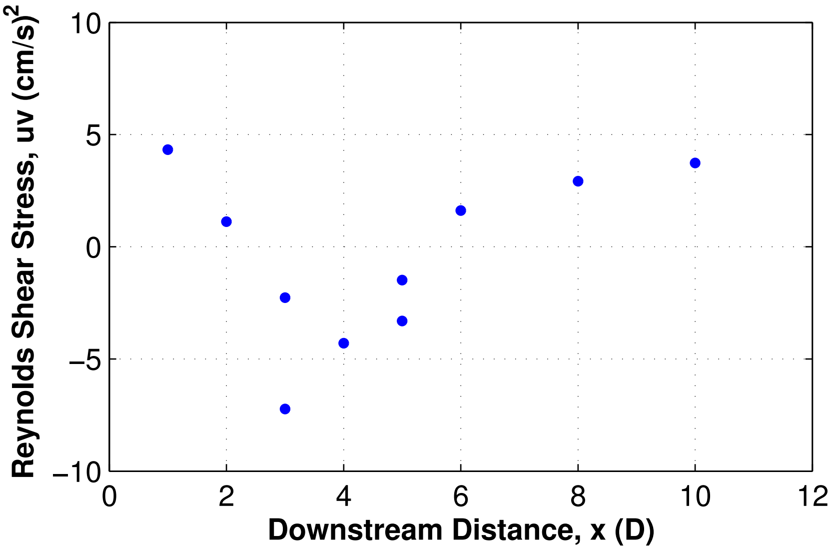
Reynolds Shear Stress, uv $(cm/s)^2$
10
5
0
–5
–10
0
2
4
6
8
10
12
Downstream Distance, x (D)

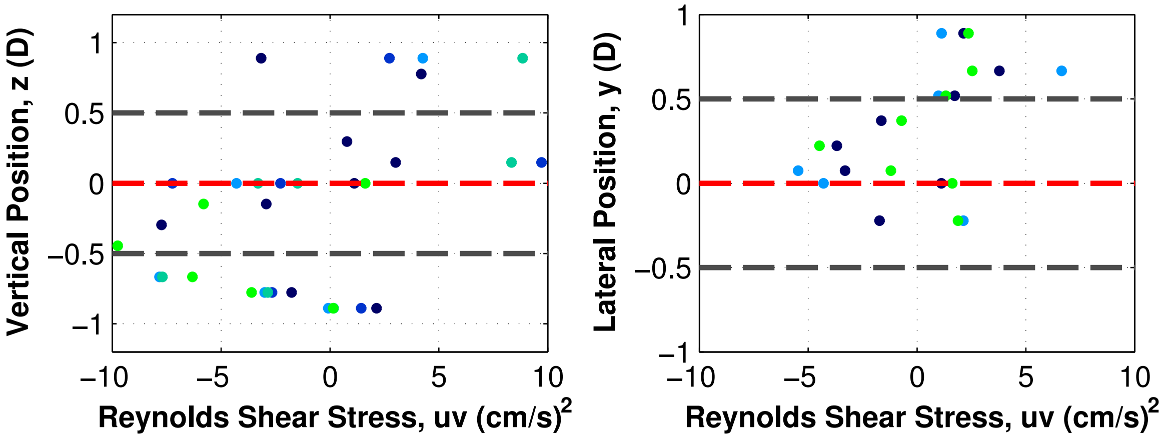
Vertical Position, z (D)
1
0.5
0
–0.5
–1
–10
–5
0
5
10
Reynolds Shear Stress, uv $(cm/s)^2$
Lateral Position, y (D)
1
0.5
0
–0.5
–1
–10
–5
0
5
10
Reynolds Shear Stress, uv $(cm/s)^2$

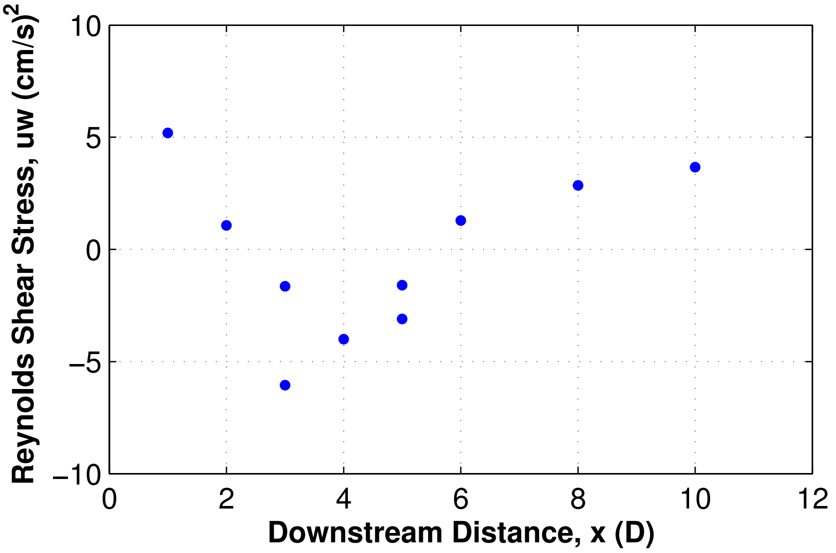
Reynolds Shear Stress, uw $(cm/s)^2$
10
5
0
–5
–10
0
2
4
6
8
10
12
Downstream Distance, x (D)

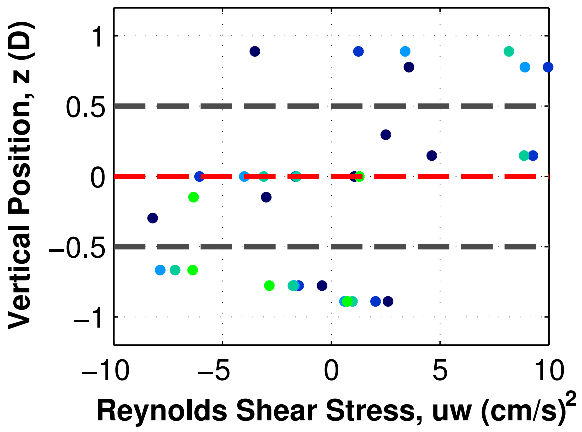
Vertical Position, z (D)
1
0.5
0
−0.5
−1
−10
−5
0
5
10
Reynolds Shear Stress, uw $(cm/s)^2$

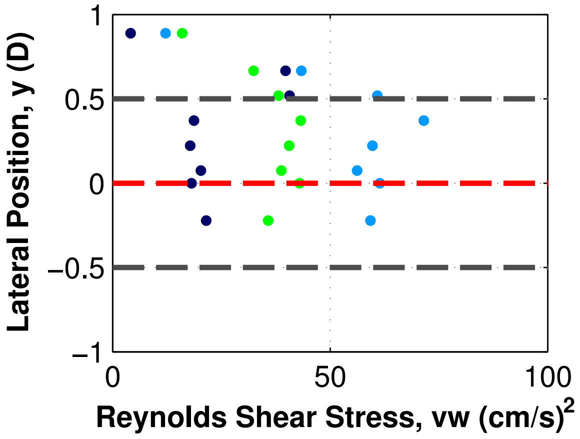
Lateral Position, y (D)
1
0.5
0
−0.5
−1
0
50
100
Reynolds Shear Stress, vw $(cm/s)^2$

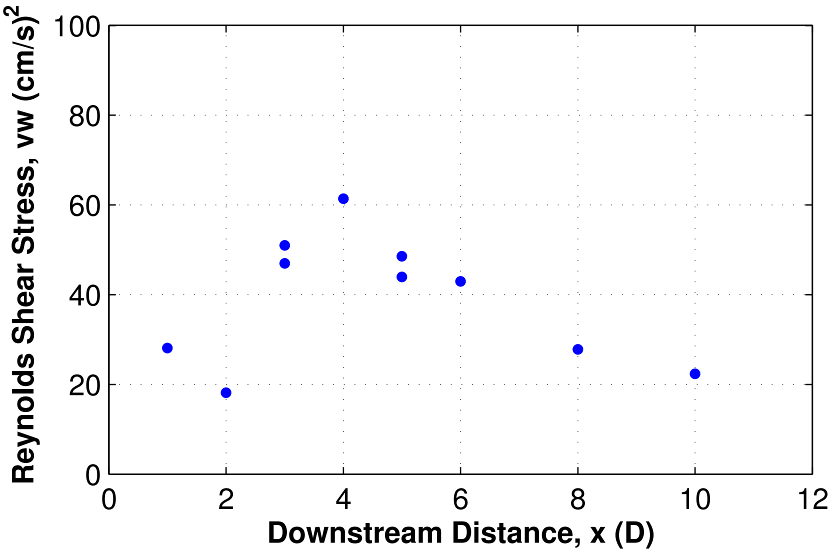
Reynolds Shear Stress, vw $(cm/s)^2$
100
80
60
40
20
0
0
2
4
6
8
10
12
Downstream Distance, x (D)

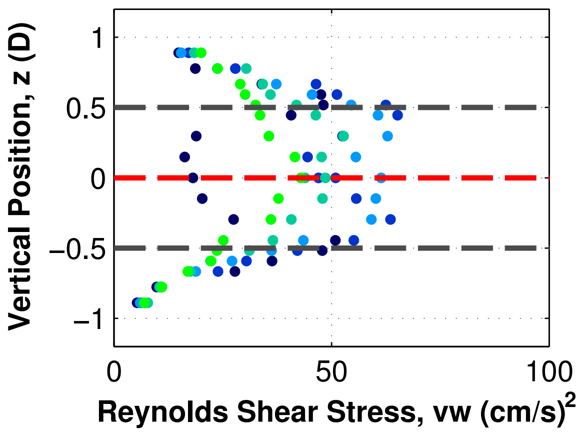
Vertical Position, z (D)
1
0.5
0
−0.5
−1
0
50
100
Reynolds Shear Stress, vw $(cm/s)^2$

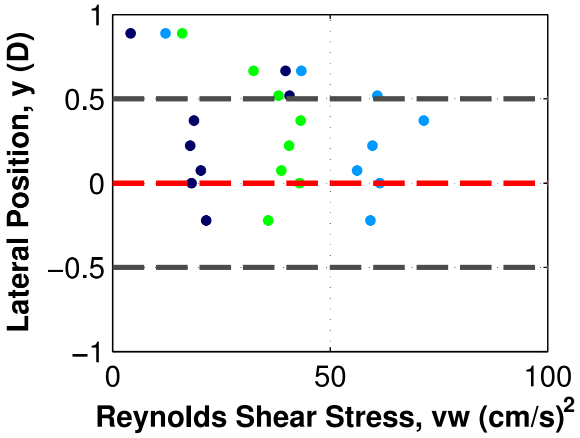
Lateral Position, y (D)
1
0.5
0
−0.5
−1
0
50
100
Reynolds Shear Stress, vw $(cm/s)^2$

6.2.6 Turbulence Intensity

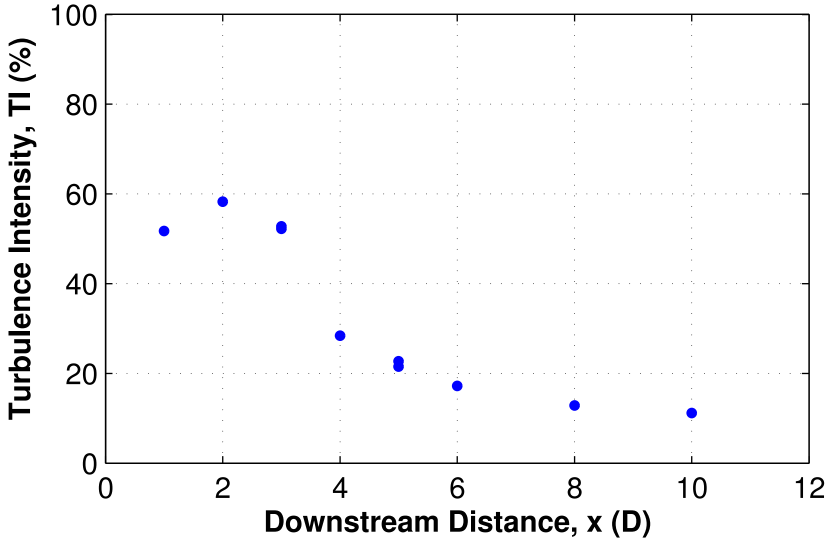

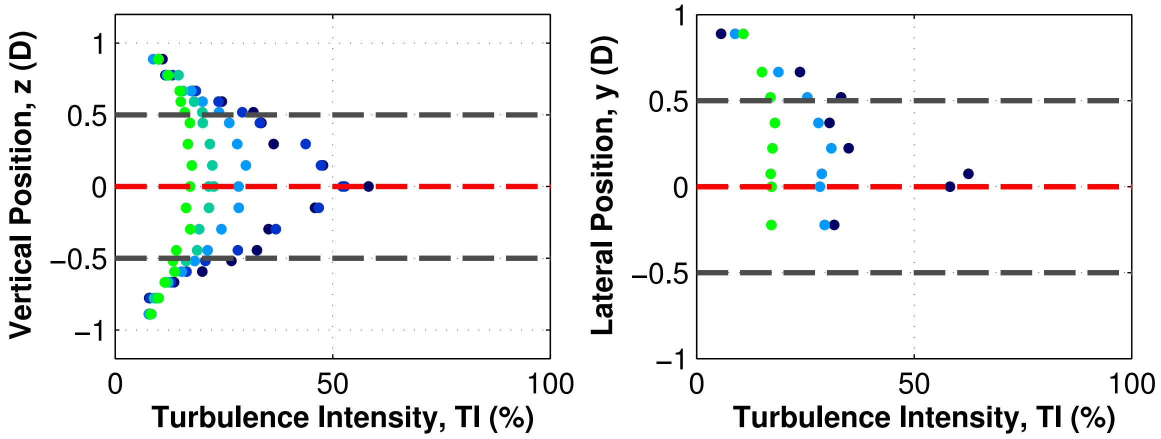

6.2.7 Turbulent Kinetic Energy

Turbulent kinetic energy has been defined as

$$TKE = \frac{1}{2}\overline{u^2 + v^2 + w^2}\ . \tag{13}$$

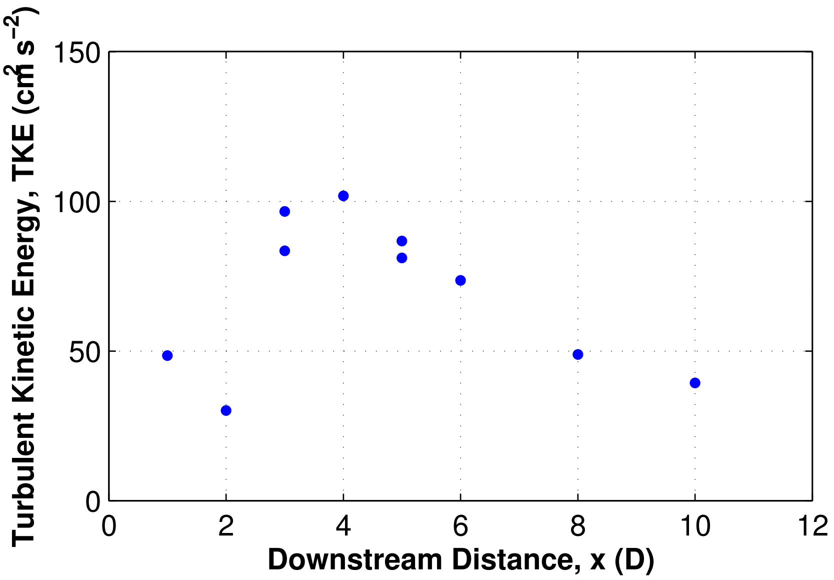
Turbulent Kinetic Energy, TKE (cm^2 s^{-2})
150
100
50
0
0
2
4
6
8
10
12
Downstream Distance, x (D)

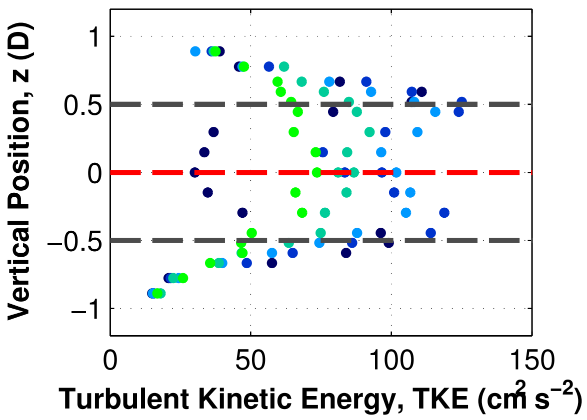
Vertical Position, z (D)
1
0.5
0
−0.5
−1
0
50
100
150
Turbulent Kinetic Energy, TKE (cm^2 s^{-2})

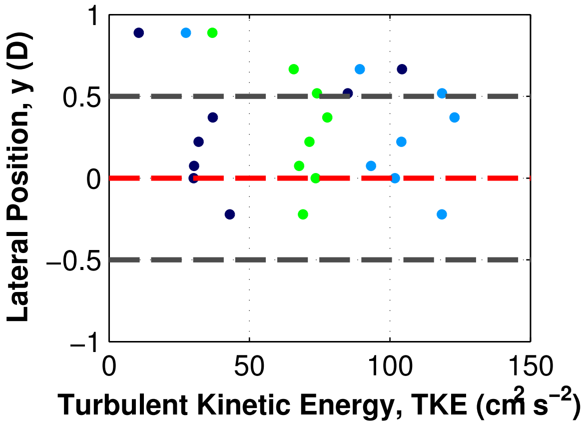
Lateral Position, y (D)
1
0.5
0
−0.5
−1
0
50
100
150
Turbulent Kinetic Energy, TKE (cm^2 s^{-2})

6.3 Test 3.2 - 0.2 m Elevation

6.3.1 Streamwise Velocity

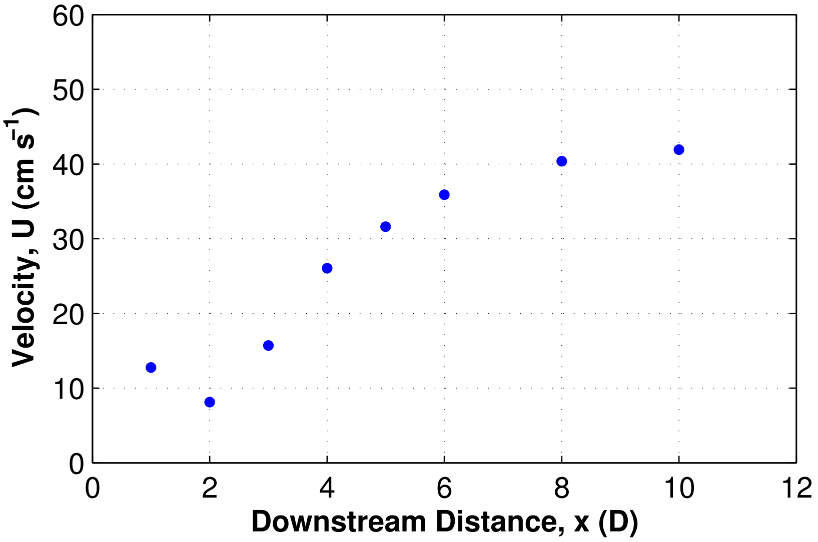

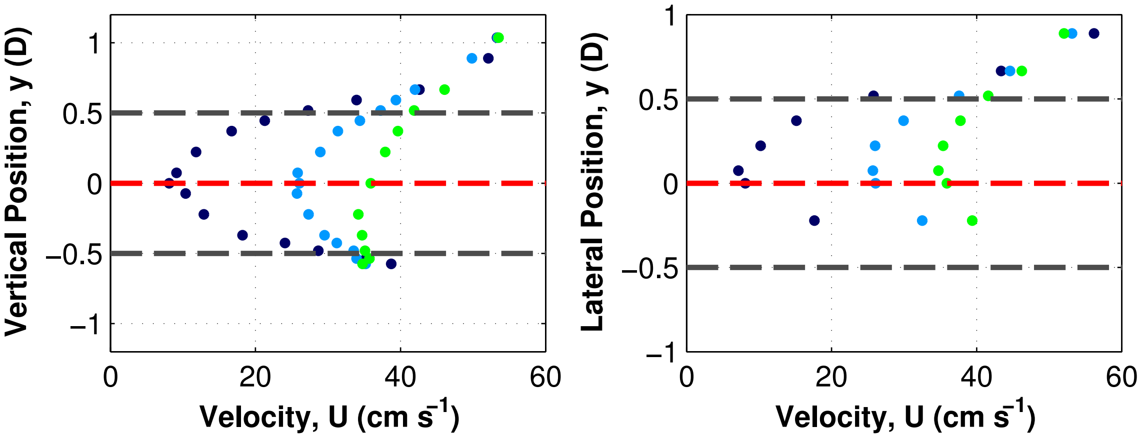

6.3.2 Lateral Velocity

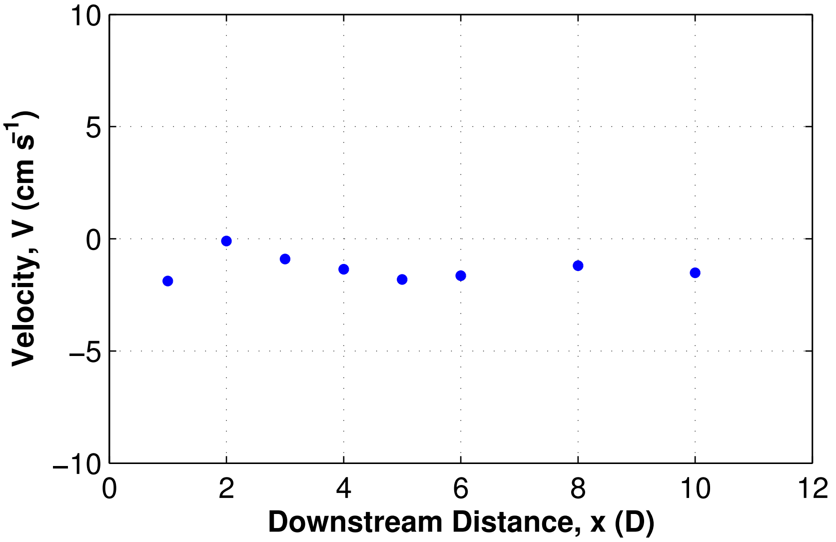

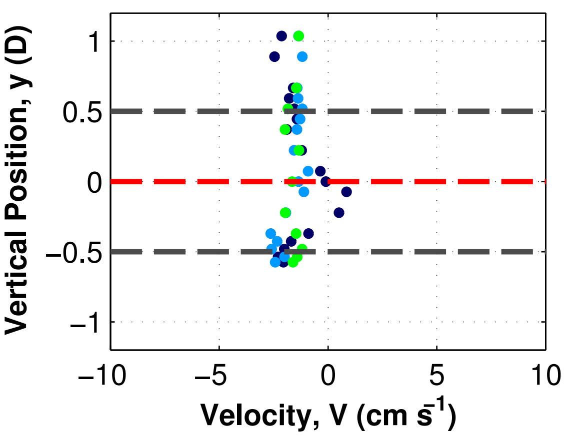

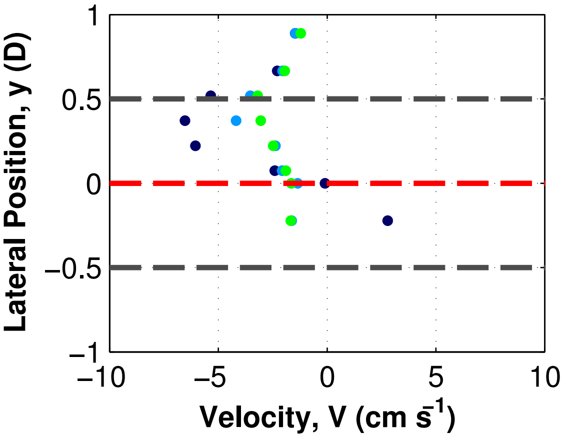

6.3.3 Vertical Velocity

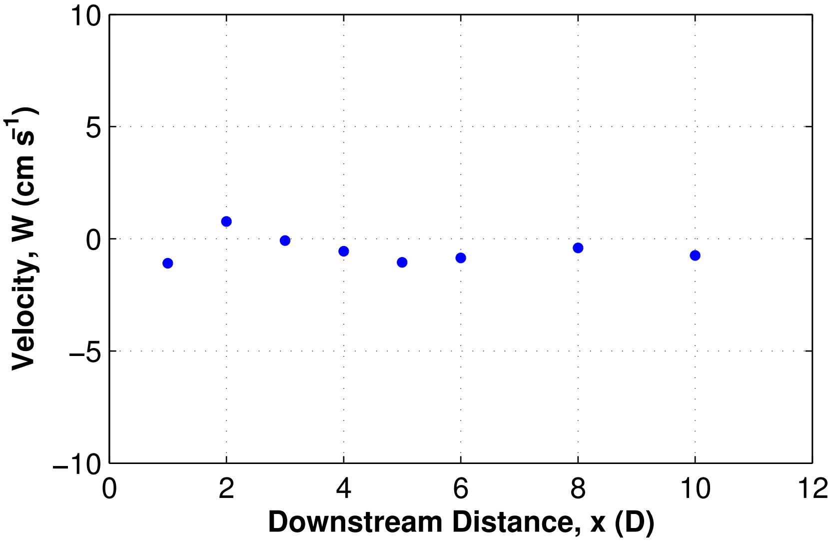

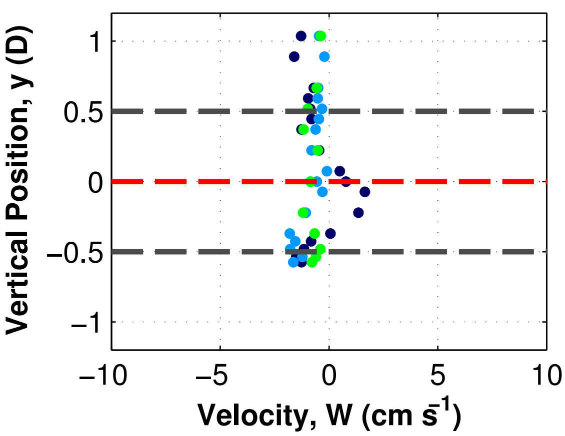

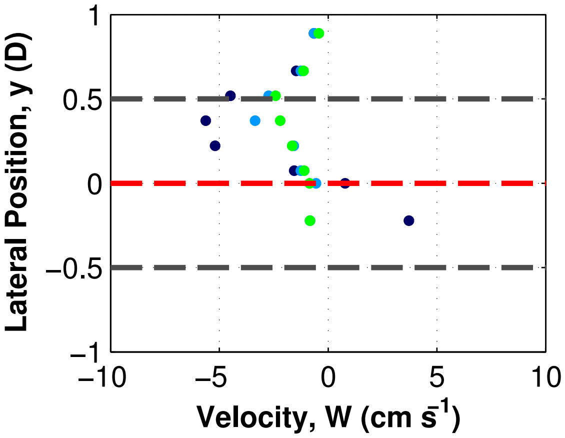

6.3.4 Normalised Streamwise Velocity Deficit

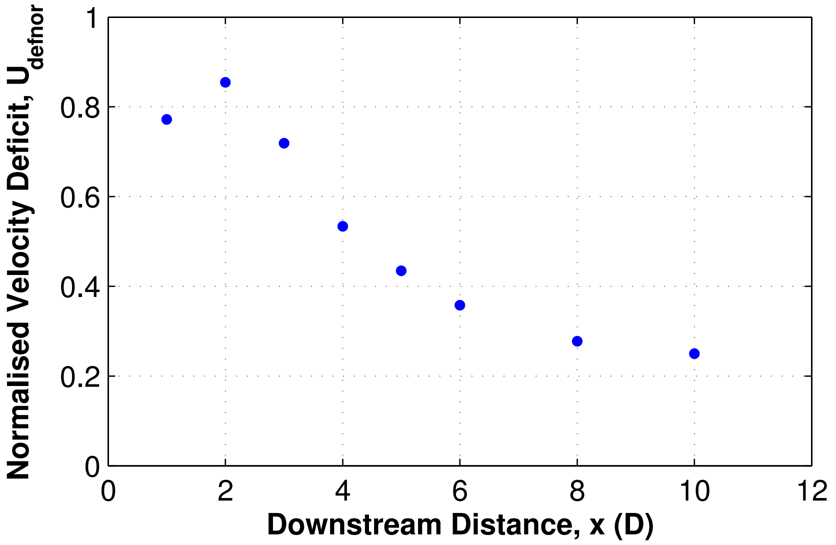

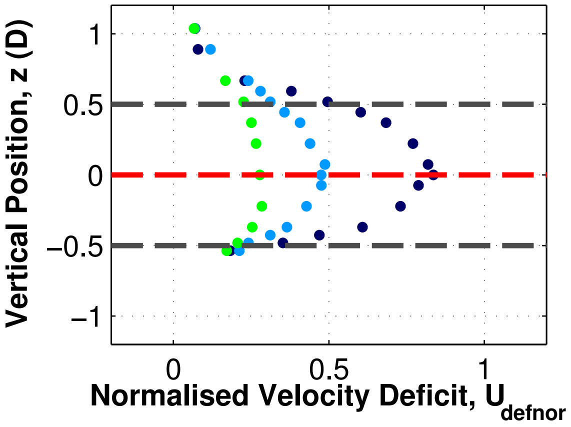

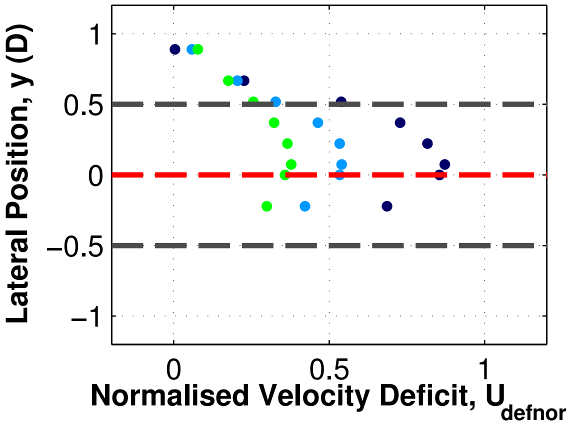

6.3.5 Reynolds stresses

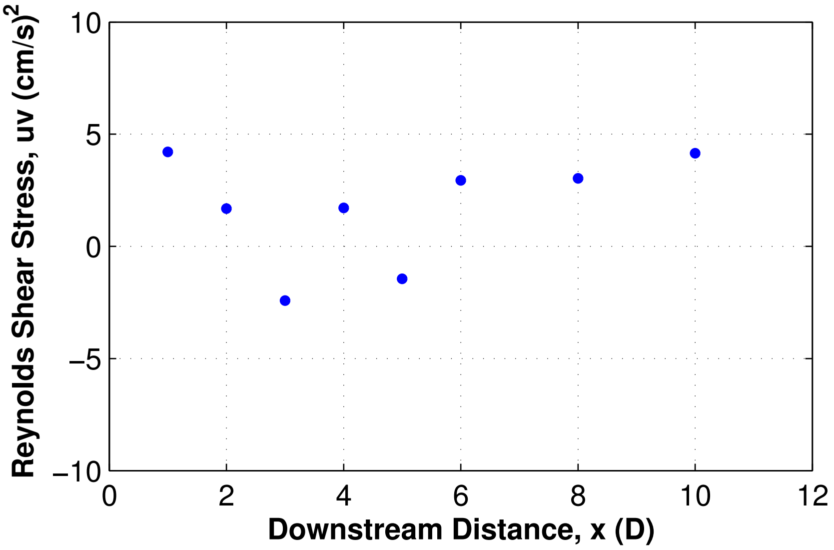

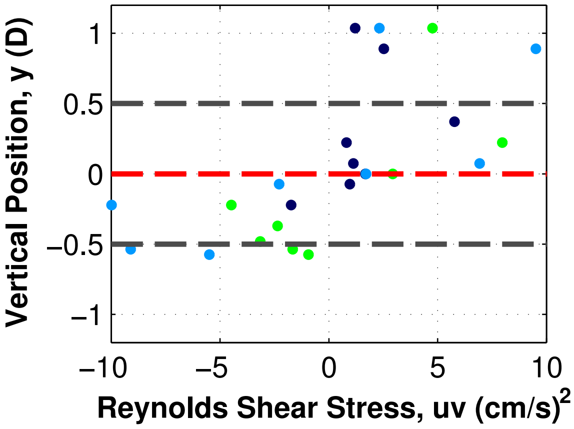

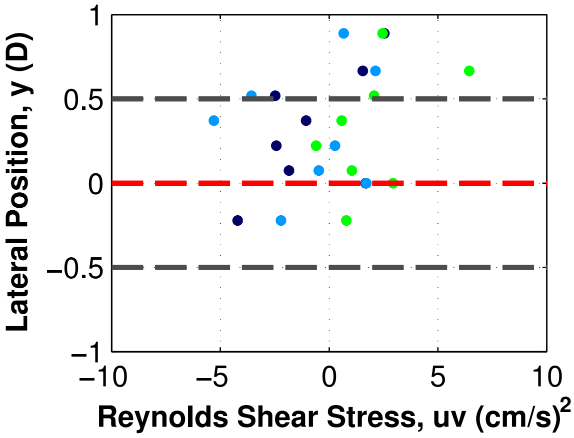

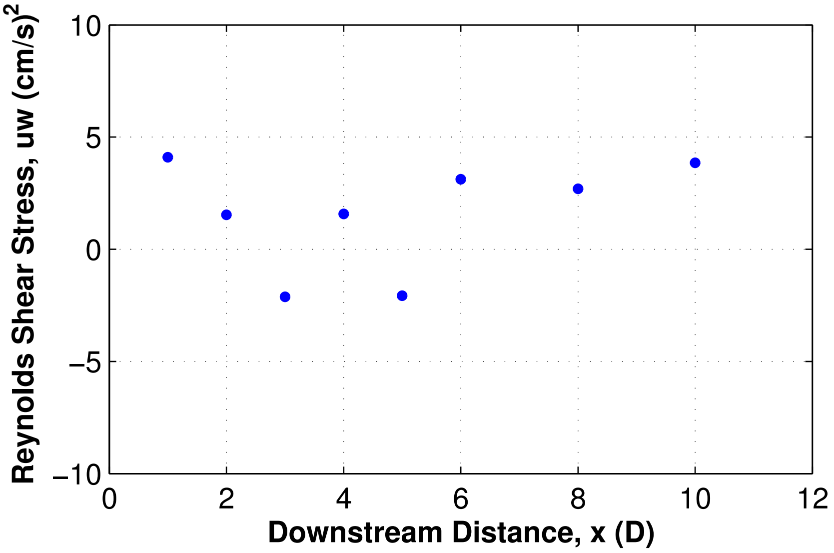
Reynolds Shear Stress, uw (cm/s)^2
10
5
0
−5
−10
0
2
4
6
8
10
12
Downstream Distance, x (D)

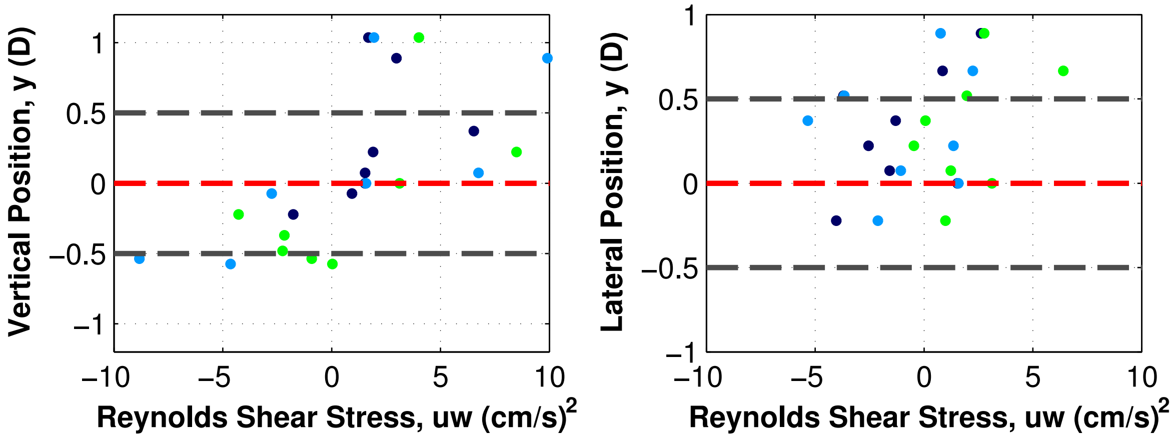
Vertical Position, y (D)
1
0.5
0
−0.5
−1
−10
−5
0
5
10
Reynolds Shear Stress, uw (cm/s)^2
Lateral Position, y (D)
1
0.5
0
−0.5
−1
−10
−5
0
5
10
Reynolds Shear Stress, uw (cm/s)^2

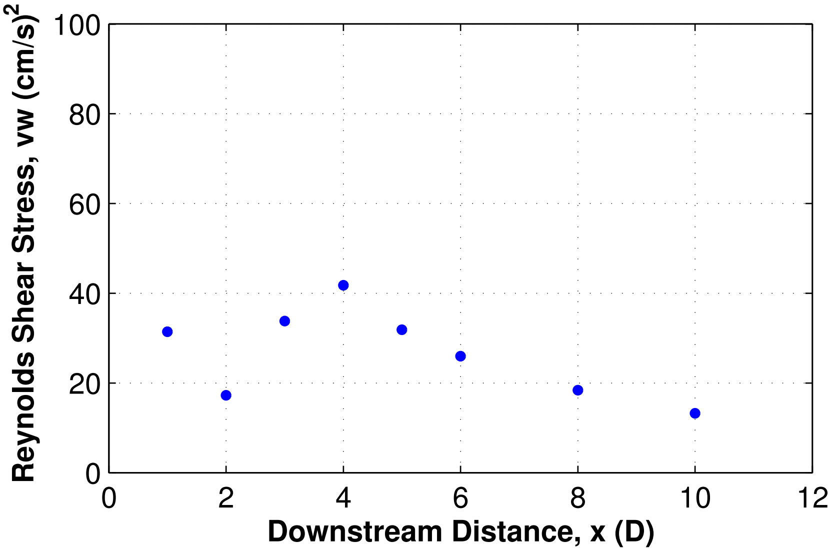
Reynolds Shear Stress, vw (cm/s)^2
100
80
60
40
20
0
0
2
4
6
8
10
12
Downstream Distance, x (D)

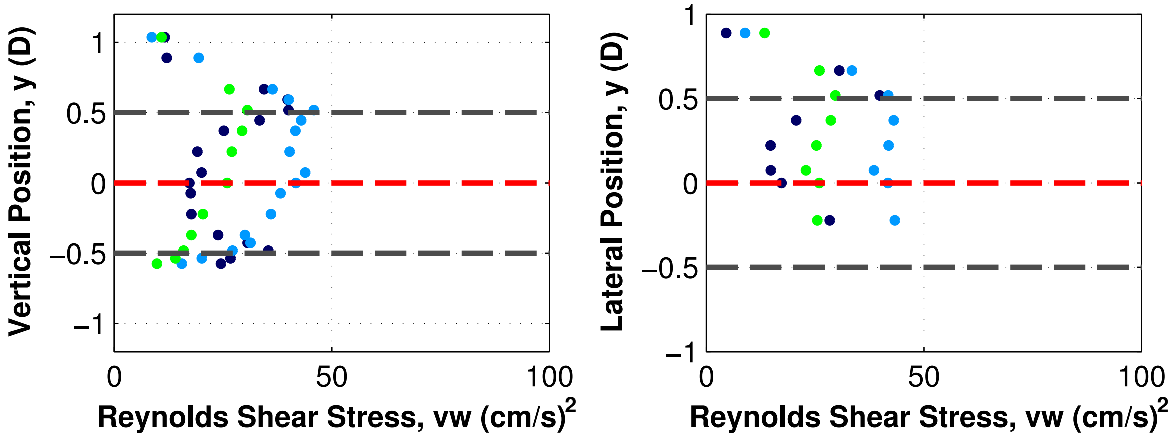

6.3.6 Turbulence Intensity

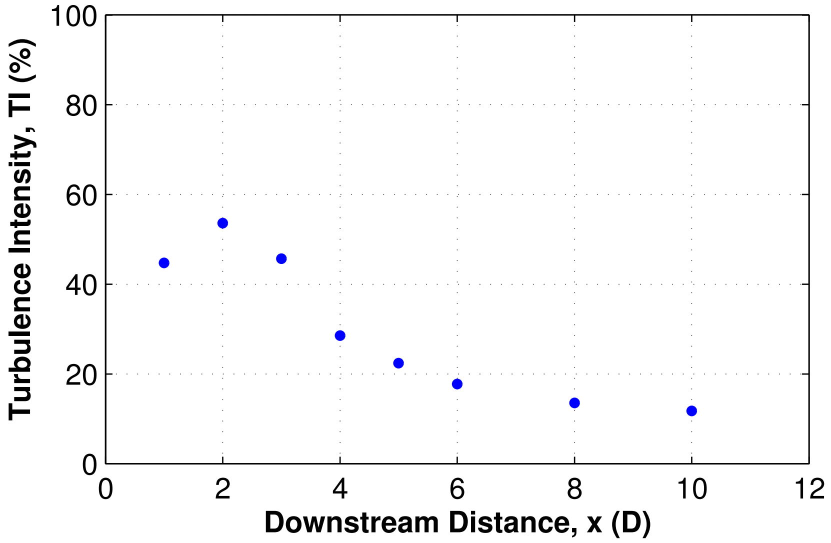

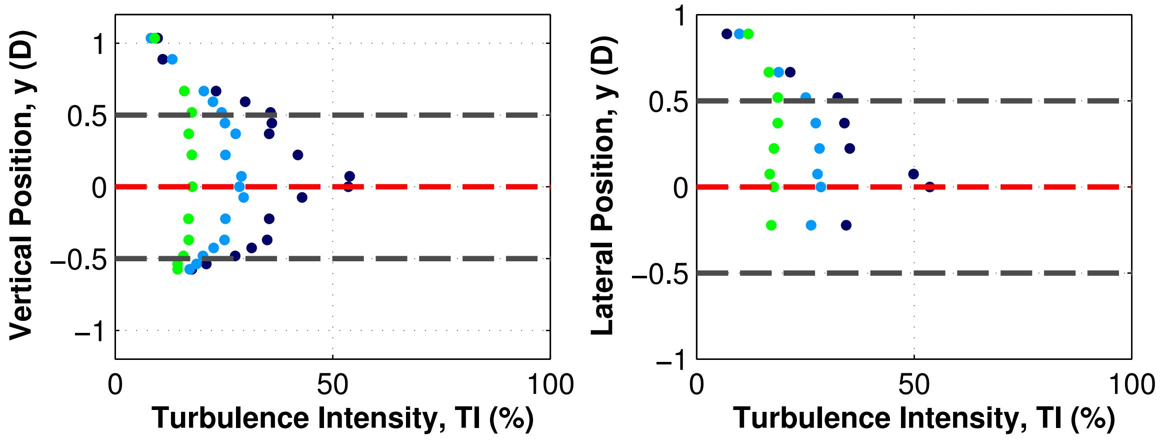

6.3.7 Turbulent Kinetic Energy